


Macrophage-inherited exosome excise tumor immunosuppression to expedite immune-activated ferroptosis

Duo Wang,^{1,2} Guanhua Qiu,^{1,2} Xiaoqi Zhu,^{1,2} Qin Wang,^{1,2} Chunyan Zhu,³ Chao Fang,³ Junjie Liu,^{1,2} Kun Zhang ,^{3,4} Yan Liu^{1,2}

To cite: Wang D, Qiu G, Zhu X, *et al.* Macrophage-inherited exosome excise tumor immunosuppression to expedite immune-activated ferroptosis. *Journal for ImmunoTherapy of Cancer* 2023;**11**:e006516. doi:10.1136/jitc-2022-006516

► Additional supplemental material is published online only. To view, please visit the journal online (<http://dx.doi.org/10.1136/jitc-2022-006516>).

DW and GQ contributed equally.

Accepted 13 April 2023

ABSTRACT

Background Immunosuppressive tumor microenvironment (ITM) remains an obstacle that jeopardizes clinical immunotherapy.

Methods To address this concern, we have engineered an exosome inherited from M1-phenotype macrophages, which thereby retain functions and ingredients of the parent M1-phenotype macrophages. The delivered RSL3 that serves as a common ferroptosis inducer can reduce the levels of ferroptosis hallmarks (eg, glutathione and glutathione peroxidase 4), break the redox homeostasis to magnify oxidative stress accumulation, promote the expression of ferroptosis-related proteins, and induce robust ferroptosis of tumor cells, accompanied with which systematic immune response activation can be realized. M1 macrophage-derived exosomes can inherit more functions and genetic substances than nanovesicles since nanovesicles inevitably suffer from substance and function loss caused by extrusion-arisied structural damage.

Results Inspired by it, spontaneous homing to tumor and M2-like macrophage polarization into M1-like ones are attained, which not only significantly magnify oxidative stress but also mitigate ITM including M2-like macrophage polarization and regulatory T cell decrease, and regulate death pathways.

Conclusions All these actions accomplish a synergistic antitumor enhancement against tumor progression, thus paving a general route to mitigate ITM, activate immune responses, and magnify ferroptosis.

INTRODUCTION

Immunosuppressive tumor microenvironment (ITM) is generally identified to be the primary reason of many immunotherapy failures associated with poor clinical benefits,^{1–4} for example, anti-PD1/L1-represented immune checkpoint blocking therapy because it can bring about poor action persistence, disable immunological surveillance, and favor immune escape. Tumor-associated macrophages (TAMs) are accepted as one component to contribute to the complex ITM,^{5,6} wherein the M2-phenotype TAMs exert the protumorigenic effect via imprisoning cytotoxic T lymphocytes (CTLs) and resisting the antitumor actions.^{7,8}

WHAT IS ALREADY KNOWN ON THIS TOPIC

⇒ M1-derived nanovesicles have been obtained based on RAW264.7 via mechanical extrusion that may pose membrane protein loss or destruction and fail to retain the functions of parent macrophages, and they have been explored in targeted delivery and combined therapy after combining targeting design and immune activation.

WHAT THIS STUDY ADDS

⇒ This study demonstrates that it is safe and feasible to integrate natural inflammation tropism-mediated accumulation, ferroptosis, redox homeostasis disruption, immunosuppressive tumor microenvironment mitigation and reactive oxygen species accumulation into one exosome-based delivery system and exert the synergistic antitumor effects.

HOW THIS STUDY MIGHT AFFECT RESEARCH, PRACTICE OR POLICY

⇒ This study provides safe, convincing and feasible data for future studies in immune-desert tumor microenvironment modulation and enhanced ferroptosis.

To address it, great efforts and advances have been made. Typically, nanotechnology-enhanced treatment methods, for example, sonodynamic therapy (SDT),^{9–11} photodynamic therapy (PDT),¹² photothermal ablation,¹³ chemodynamic therapy (CDT),¹⁴ radiotherapy,¹⁵ radiofrequency ablation,^{16–17} etc, have been developed to activate systematic immune responses and mitigate ITM via promoting M2-phenotype TAMs' polarization and elevating cytokine secretions and CTLs infiltrations. Actually, reactive oxygen species (ROS) in SDT, PDT, or CDT are the primary factor that drives protumorigenic M2 TAM polarization into antitumorigenic M1 ones,^{4,18,19} which also have been validated to drive the differentiation and proliferation of stem cells.^{20–22} Therein, the multiple combined actions significantly inhibited tumor progression and metastasis especially



© Author(s) (or their employer(s)) 2023. Re-use permitted under CC BY-NC. No commercial re-use. See rights and permissions. Published by BMJ.

For numbered affiliations see end of article.

Correspondence to

Professor Kun Zhang;
zhang1986kun@126.com

Professor Yan Liu;
liuyan@gxmu.edu.cn

after combining with immunotherapy or tumor microenvironment modulation. Besides nanotechnology-enhanced treatment methods, nanotechnology-enabled death pathway regulation is another route to dictate ITM and immunotherapy. Generally, apoptosis, ferroptosis, and pyroptosis are three typical programmed death pathways,^{23–26} wherein ferroptosis has been documented to induce robust immune responses akin to pyroptosis.^{27–30} Therefore, nanotechnology-modulated ferroptosis is also expected to reverse ITM and enhance immunotherapy.

In the aforementioned nanotechnology-encouraged strategies, highly efficient nanodelivery of functional agents is an indispensable prerequisite. Various active or negative targeting strategies have been attempted to enhance the accumulation for magnifying the diagnosis or/and treatment outcomes,^{31–33} for example, acceptor-mediated active targeting,³¹ ultrasound or radiofrequency-enhanced permeability,^{33–35} etc. With inheriting from the parent cancer cells or inflammatory cells, their extracellular vesicles or extrusion-engineered nanovesicles are also imparted with high tropism and spontaneous homing ability,³⁶ which are highly desirable for specifically delivering drugs, genes, proteins, or other functional nanoparticles.^{37–40} Nevertheless, the structure destruction and size shrinkage during the mechanical extrusion of nanovesicles inevitably cause the loss of genetic materials or information (proteins, cytokines, RNA, etc), disabling the extruded nanovesicles to completely retain the functions of their parent exosomes, let alone the functions of inflammatory progenitor cells.^{41–43}

In this report, we engineered M1 macrophage-inherited exosome (M1-Exo) that loaded the ferroptosis inducer (ie, RSL3) (RSL3-carried exosome (RSL3-Exo)) for elevating RSL3 retention in tumor and excising ITM, which reinforced the immune responses to cooperatively favor ferroptosis. Herein, the loaded RLS3 as the ferroptosis inducer can decrease glutathione (GSH) level, downregulate glutathione peroxidase 4 (GPX4) and expedite ROS accumulation in tumor.^{44–45} More significantly, M1 macrophage-represented immune cells that outperform tumor cells in activating or enhancing antitumor immunity are much preferable to engineer exosomes. The M1-Exos are expected to retain the ingredients and functions of M1 macrophages for spontaneous homing to tumor, activating immune responses and alleviating ITM since the production process fails to experience the extrusion-caused structure destruction and component loss that nanovesicles encountered.^{46–49} Contributed by the ITM mitigation and homing-mediated high RSL3 accumulation caused by such M1-Exos, the protumorigenic M2 TAM polarization into antitumorigenic M1 ones, as well as regulatory T-cell (Treg) decrease, was reached (figure 1). They were validated to significantly enhance ferroptosis via provoking systematic immune responses and regulating ferroptosis-related protumorigenic and antitumorigenic protein expressions, as indicated in figure 1. The macrophage-inherited exosome engineering provides a general route to manipulate the immune microenvironment and enhance ferroptosis or other death pathway-activated immune response for resisting tumor progression.

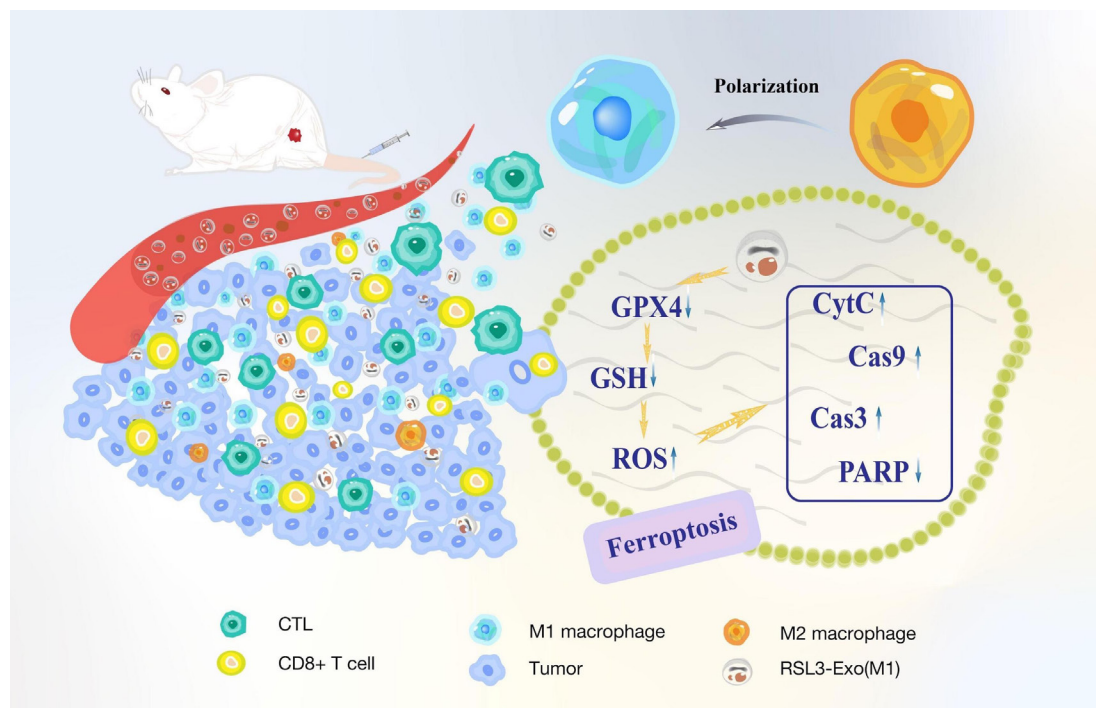


Figure 1 Schematic explaining how macrophage-inherited exosome executioners mitigate ITM to expedite immune-activated ferroptosis through promoting M2 macrophage polarization into M1, and downregulating GPX4 and GSH, increasing ROS level, promoting CD8+ T and CTL infiltrations and decreasing Tregs. CTL, cytotoxic T lymphocyte; GPX4, glutathione peroxidase 4; GSH, glutathione; ITM, immunosuppressive tumor microenvironment; ROS, reactive oxygen species; Treg, regulatory T cell.

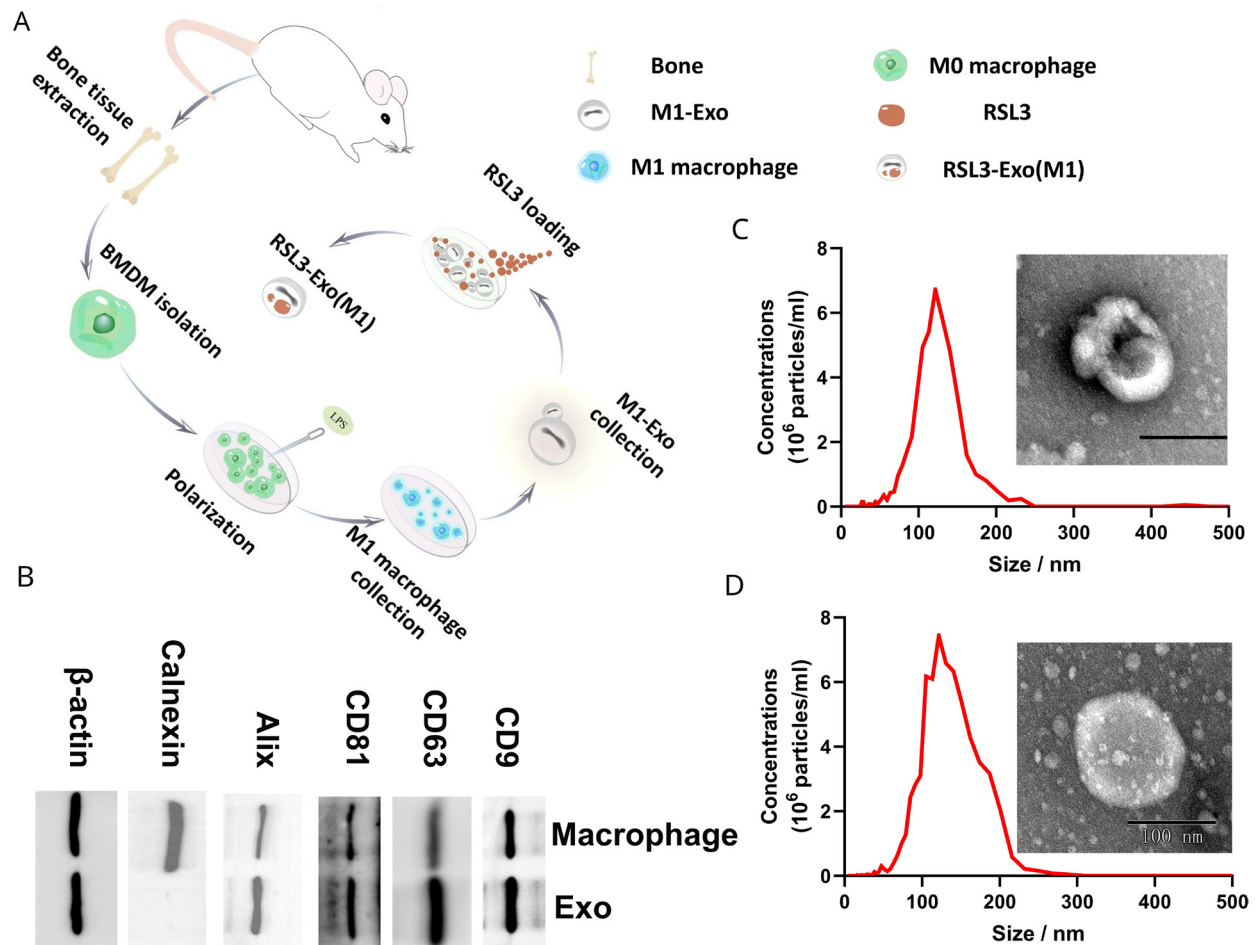


Figure 2 Characterization and test on the Exo and RSL3-Exo. (A) The synthetic procedure of Exo and RSL3-Exo. (B) Western blot patterns of parent macrophage and secreted Exo. (C,D) Size distribution and the corresponding TEM images of Exo (C) and RSL3-Exo (D) via nanoparticle tracking analysis. BMDM, bone marrow-derived macrophage; RSL3-Exo, RSL3-carried exosome; TEM, transmission electron microscopy.

RESULTS AND DISCUSSION

M1-Exo collection and RSL3-Exo engineering

The M1-Exo and RSL3-Exo are acquired according to the sequential route, as shown in [figure 2A](#). In detail, bone marrow-derived macrophages were isolated from bone tissue of mice, and then the stimulated by lipopolysaccharide to obtain M1-phenotype macrophages, followed by M1-Exo production and collection. Ultimately, RSL3 was added and enter Exo to obtain RSL3-Exo. Western blot (WB) analysis indicates the secreted exosomes retain the proteins of their parent M1-phenotype macrophages, as shown in [figure 2B](#), denoting that the M1-Exo is ensured to have the ability of spontaneous homing to tumor. The size of Exo is determined to be around 100 nm by the transmission electron microscopy observation and nanoparticle tracking analysis (NTA), as evidenced in [figure 2C](#), and the loading percentage of RSL3 is determined to be 4.76%. Intriguingly, after loading RSL3, the obtained RLS3-Exo shows the approximately identical size to Exo ([figure 2D](#)), indicating RSL3 entrapment fails to alter the Exo size.

In vitro ferroptosis test induced by RSL3-Exo

High accumulation of functional agents including drugs or probes is the precondition of highly efficient diagnosis or treatment of one lesion. Appealingly, the spontaneous homing to tumor is anticipated to be imparted with Exo and RSL3-Exo since they retain the parent proteins of M1 macrophages capable of spontaneously approaching and entering tumor tissues.^{50 51} As expected, a large number of RSL3-Exo infect 4T1 tumor cells, and as the incubation time is prolonged, more RSL3-Exos target and are retained in 4T1 cells, as displayed in online supplemental figure S1.

To investigate ferroptosis induced by RSL3-Exo, some typical markers mattering ferroptosis was inspected. It has been extensively accepted that ferroptosis is characterized with lipid peroxidation, GSH decrease and GPX4 downregulation.^{30 44} After careful examinations, it is found that Exo alone fails to induce lipid peroxidation, while RSL3-contained groups result in the tremendously increased lipid peroxidation ([figure 3A](#)), which can be attributed to the fact that RSL3 as the specific ferroptosis inducer initiates the ferroptosis process. Subsequently,

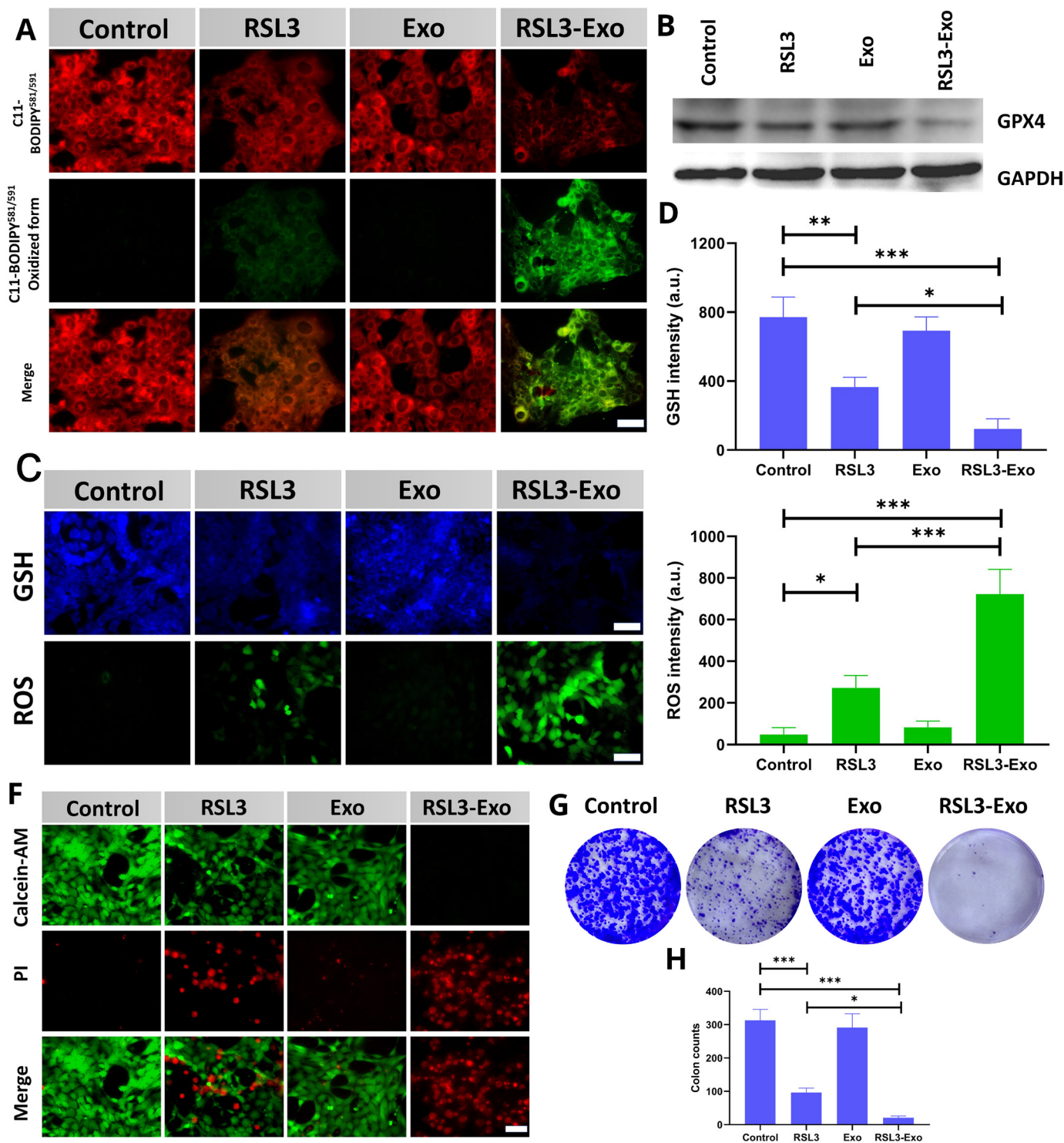


Figure 3 In vitro tests on ferroptosis via detecting its biomarkers or pathological characteristics. (A) CLSM images of 4T1 cells stained with lipid peroxidation probe (ie, C11 BODIPY 581/591) after different treatments in their corresponding groups. (B) WB patterns of 4T1 cells after different treatments in their corresponding groups for determining the expression of Ferroptosis biomarker (GPX4). (C) CLSM images of 4T1 cells stained with GSH and ROS indicators after different treatments in their corresponding groups. (D,E) Quantitative levels of ROS and GSH in 4T1 cells after different treatments in their corresponding groups, which was obtained from their CLSM images (C). (F) CLSM images of 4T1 cells stained with live/dead dyes (ie, PI/calcein-AM) after different treatments in their corresponding groups, where PI-stained red cells and calcein-AM-stained green cells indicate dead and live cells, respectively. (G,H) Clone tests for detecting proliferation level of 4T1 cells after different treatments in their corresponding groups including via optical microscopic observation (G) and quantitative verification (H). Scale bar: 50 μ m. Data are expressed as mean \pm SD (n=3). One-way analysis of variance was used to analyze the statistical differences between two groups. *P<0.05, **P<0.01, ***P<0.001. CLSM, confocal laser scanning microscopy; GPX4, glutathione peroxidase 4; GSH, glutathione; PI, propidium iodide; ROS, reactive oxygen species; WB, western blot.

WB result reveals that the ferroptosis launching in RSL3-contained groups further gives rise to GPX4 downregulation (figure 3B). In light of the close correlation between GPX4 and GSH, the GPX4 downregulation also implies GSH decrease,⁴⁴ which will benefit ROS accumulation via the redox balance disruption.⁹ After staining with GSH and ROS indicators postcorresponding treatment in different groups, RSL3 alone is found to remarkably decrease GSH level. Once combined with Exo-mediated active targeting, more RSL3 molecules are delivered into 4T1 cells, making RSL3-Exo harvest the most descendent magnitude of GSH, as confirmed by the confocal laser scanning microscopy (CLSM) observation and semi-quantitative analysis (figure 3C,D). On the contrary, the RSL3-Exo group receives the highest ROS accumulation (figure 3C,E). All these variations of ferroptosis hall-markers convincingly suggest the significantly enhanced ferroptosis induced by such RSL3-loaded exosomes and M1-Exo (ie, RSL3-Exo).

To explore how the enhanced ferroptosis-arised death pathways exert the influencing action on antitumor outcome, *in vitro* 4T1 death induced by RSL3-Exo was surveyed. First, propidium iodide (PI) and calcein-AM, two dyes for labeling dead and live cells, were harnessed to stain 4T1 cells after different treatments so as to differentiate the dead cells.⁵² Contributed by the most ROS accumulation, green fluorescence representing live cells completely recedes, and red fluorescence representing dead cells almost illuminate all cells (figure 3F), suggesting that RSL3-Exo treatment indeed orients the ferroptosis pathway to kill cancer cells. Subsequently, clone formation assay unveiling RSL3 brings about the prominently decreased proliferation of 4T1 cells, while the Exo-enabled high RSL3 accumulation further inhibits the proliferation, which encourages the highest inhibition rate of 4T1 cells, as evidenced in figure 3G,H. Similar results are obtained in the flow cytometry (FCM) test, wherein PI and annexin V were leveraged to stain dead and live cells and differentiate the phase. Results show that RSL3-Exo treatment leads to the highest death percentage (above 70%) compared with RSL3 alone (approximately 40%) or Exo alone (below 20%) (online supplemental figure S2). Actually, such RSL3-loaded exosomes and M1-Exo (ie, RSL3-Exo) can be extended to other tumors, for example, colorectal cancer. To verify it, colorectal cancer cell line (CT26) serves as the model, and RSL3-Exo also poses GSH drop and ROS rise via activating the ferroptosis pathway (online supplemental figure S3), triggering the most deaths of CT26 cells, as indicated by the CLSM observation and clone formation assay (online supplemental figures S4 and S5).

In vivo antitumor assessment using RSL3-Exo-enhanced ferroptosis

Inspired by the appealing results *in vitro*, *in vivo* distribution and antitumor tests were carried on. To visually trace the accumulation and distribution of RSL3-Exo, *in vivo* animal fluorescence imaging was implemented and

a near-infrared fluorescence dye (indocyanine green (ICG)) featuring high light penetration depth was used instead of RSL3. As the observation time proceeds, it is found that more and more ICG-labeled Exos progressively enter and accumulate in the tumor, reaches the highest level at 18 hours post injection, and then metabolism is initiated, as indicated in figure 4A. Astonishingly, even though 48 hours has passed away, there are still lots of Exo retention in the tumor (figure 4A,B), which will favor the *in vivo* RSL3-Exo-enhanced ferroptosis antitumor outcome.

The *in vivo* antitumor procedure is outlined in figure 4C, where once intravenous injection per 2 days with five administered in total was set. According to the time-dependent tumor growth profiles of each group (figure 4D,E), both RSL3-contained groups (ie, RSL3 alone and RSL3-Exo) delay tumor growth. In particular, the two actions of Exo homing-mediated high accumulation and RSL3-enabled ferroptosis synergize to contribute to the largest inhibitory rate. Intriguingly, Exo alone also inhibit tumor progression to some extent, which uncovers that Exo alone probably activates or enhances innate immune responses. The activated innate immunity even overtakes RSL3-induced adaptive immune response in resisting tumor growth. Thereby, besides the two actions (ie, Exo homing-mediated high accumulation and RSL3-enabled ferroptosis), M1-Exo-arised innate immunity and ferroptosis-activated adaptive immunity also contributed to the significantly elevated antitumor activity. More significantly, since the exosomes inherit M1 macrophages, they are ensured to impart with the ability to regulate ITM to further enhance the innate and adaptive immune responses.

At the end of the experimental period, tumors in each group were collected and photographed, and their weights were obtained. In accord with the trend of tumor growth profiles in the four groups, RSL3 alone and Exo alone delay the tumor growth, while RSL3-Exo harvests the lowest tumor weight (figure 4F,G). The alleviation trend of tumor burden is also consistent with the prolonging magnitude of mice survival in different groups, wherein RSL3-Exo also acquired the longest survival rate (figure 4H). During the experimental period, no fluctuation of body weight of tumor-bearing mice in each group is observed (online supplemental figure S6), ensuring the treatment safety. Pathological examinations proceeded, and cancer cell density and more terminal deoxynucleotidyl transferase-mediated nick end labeling apoptosis are accessible to the most optical antitumor group (RSL3-Exo), as shown in online supplemental figure S7.

To unmask whether the ferroptosis pathway activation was responsible for the excellent antitumor consequence, some typical ferroptosis-related proteins were examined.³⁰ As can be found in figure 4I, some proapoptotic proteins, including cytc, caspase-3 and caspase-9 in the four groups, are gradually upregulated, which matches the trend of antitumor outcome: control < RSL3

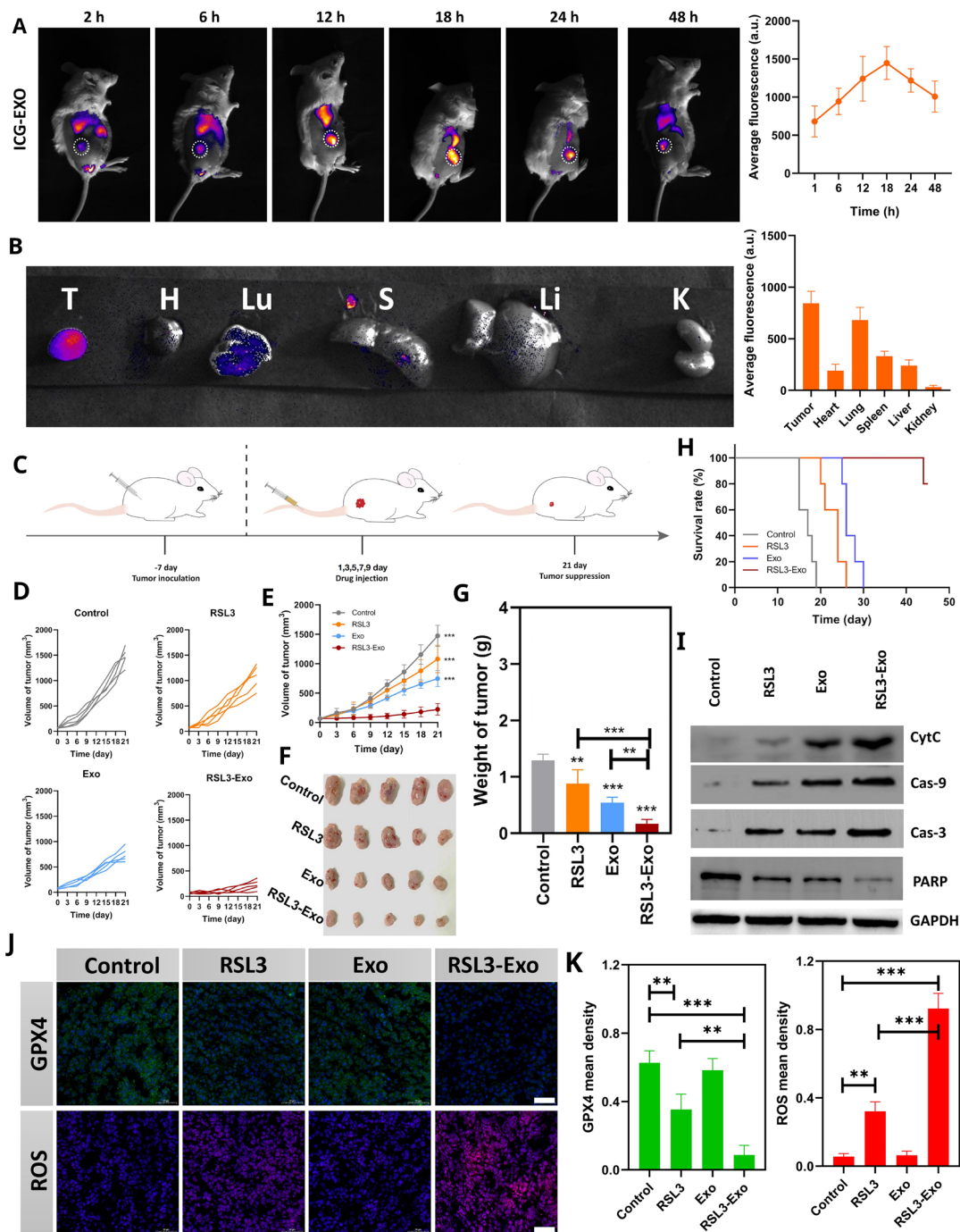


Figure 4 In vivo homing and antitumor test via induced ferroptosis and enhanced immune responses. (A) In vivo time-dependent fluorescence images and the corresponding average fluorescence intensities of 4T1 tumor-bearing mice after intravenously injecting RSL3-Exo. (B) Ex vivo fluorescence images and the corresponding average fluorescence intensities of isolated tumors and main organs from 4T1 tumor-bearing mice after 48 hours postintravenous injection of RSL3-Exo. Data are expressed as mean \pm SD ($n=3$). (C) The operation procedure of in vivo antitumor experiment on BALB/C female 4T1 tumor-bearing mice. (D) The time-dependent tumor growth profile of each mouse in each group after the corresponding treatments. (E) The average time-dependent tumor growth profiles of mice in each group after the corresponding treatments. (F,G) Digital photos (F) and weights (G) of isolated tumors from 4T1 tumor-bearing mice after the corresponding treatments in each group. Data are expressed as mean \pm SD ($n=5$). (H) The time-correlated survival rate of 4T1 tumor-bearing mice after the corresponding treatments in each group. (I) In vivo WB bands for determining various death-related proteins in 4T1 tumors isolated from 4T1 tumor-bearing mice after the corresponding treatments in each group. (J,K) CLSM images (J) and quantitative data (K) of 4T1 tumor slices stained with GPX4 and ROS immunofluorescence indicators, respectively, which were collected from 4T1 tumor-bearing mice that experienced different treatments in the corresponding groups. Scale bar: 50 μ m. Data are expressed as mean \pm SD ($n=3$). One-way analysis of variance was used to analyze the statistical differences between two groups. ** $P<0.01$, *** $P<0.001$. CLSM, confocal laser scanning microscopy; GPX4, glutathione peroxidase 4; ROS, reactive oxygen species; RSL3-Exo, RSL3-carried exosome; WB, western blot.

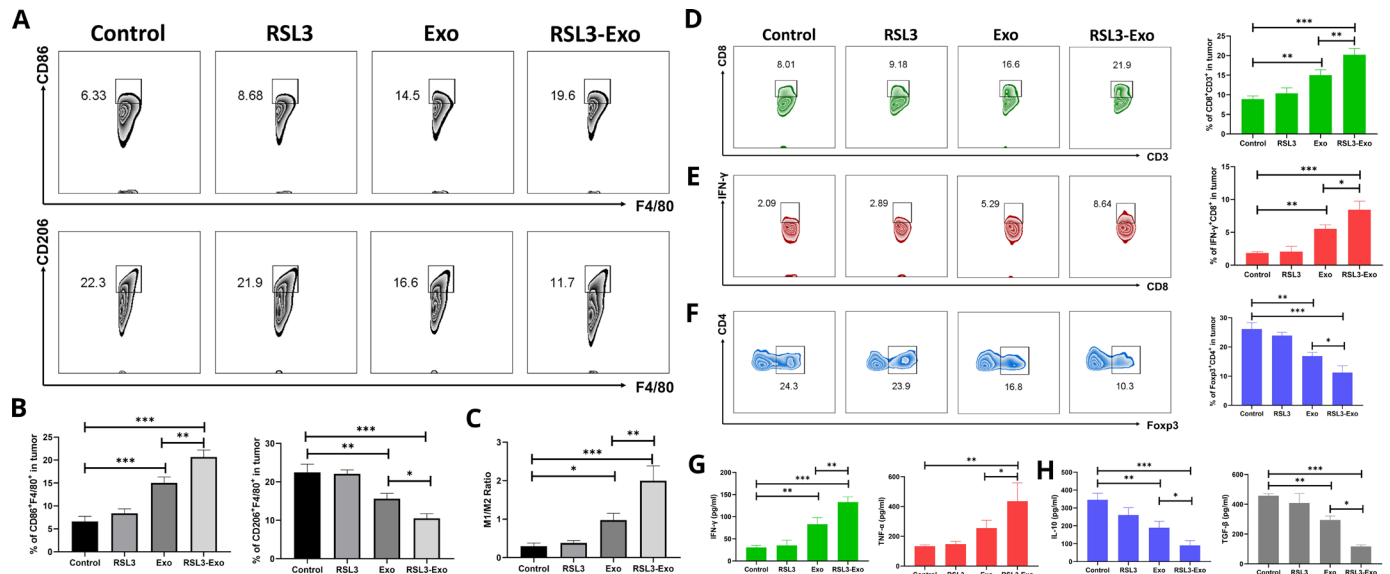


Figure 5 Mechanism exploration on ferroptosis-unlocked ITM alleviation and immune activation by such macrophage-inherited exosome executioners. (A) FCM patterns and (B) quantitative percentages of CD86+ (M1-like TAMs) and CD206+ cells (M2-like TAMs) gating from CD11b+F4/80+ macrophages in 4T1 tumor after 21 days postcorresponding treatment in different groups. (C) The ratio of M1 TAMs to M2 TAMs in 4T1 tumor after 21 days postcorresponding treatment in different groups. (E–G) FCM patterns and quantitative percentages of CD3+CD8+ T cells (D), IFN-γ+CD8+CD3+ T cells (E) and Tregs (FOXP3+CD4+CD3+) (F) in 4T1 tumor after 21 days postcorresponding treatment in different groups. (G,H) Secretion levels of antitumor cytokines (ie, IFN-γ and TNF-α) (G) and protumorigenic ones (ie, IL-10 and TGF-β) (H) in 4T1 tumor after 21 days postcorresponding treatment in different groups. Data are expressed as mean±SD (n=3). One-way analysis of variance was used to analyze the statistical differences between two groups. *P<0.05, **P<0.01, ***P<0.001. FCM, flow cytometry; IFN-γ, interferon gamma; IL, interleukin; ITM, immunosuppressive tumor microenvironment; TAM, tumor-associated macrophage; TGF-β, transforming growth factor beta; TNF-α, tumor necrosis factor alpha; Treg, regulatory T cell.

alone<Exo alone<RSL3Exo. In contrast, the antiapoptotic protein (eg, PARP(poly ADP-ribose polymerase)) is downregulated. Additionally, evidence of direct ferroptosis is obtained, and two typical ferroptosis hallmarks, that is, GPX4 and ROS, are highly expressed as the anti-tumor outcome varies, as demonstrated by the signal comparison of green fluorescence-positive GPX4 and red fluorescence-positive ROS among various groups (figure 4J,K).

Survey on ITM mitigation and immune activation by such RSL3-loaded exosomes and M1-Exo

As stated previously, M1-Exo also exerted the robust anti-tumor outcome, and thus is speculated to excise ITM to enhance the RSL3 ferroptosis-activated immune responses. To understand it, immune-related explorations were made. First, the protumorigenic M2-type macrophage polarization was assessed since it is one main target of complex ITM. FCM analysis shows that M1-Exo remarkably raises the percentage of M1 macrophages and reduces the proportion of M2 macrophages in tumor compared with control and RSL3 alone, as shown in figure 5A,B. Notably, RSL3-induced ferroptosis is also responsible for M2-type macrophage polarization, akin to reports.^{53 54} On this account, the highest level of M1 macrophages and the lowest level of M2 macrophages are reached, and the ratio of M1 macrophages to M2 ones is raised to the highest level in such RSL3-loaded and M1-Exo (figure 5C). This phenomenon adequately suggests that M1 macrophage-derived exosomes can expedite the polarization

of protumorigenic M2-type macrophages into antitumorogenic M1-like ones, probably through releasing the cytokines, and propel ITM mitigation.

Furthermore, the immunotherapy executor, CD8+ T lymphocytes, were tracked. The infiltrated percentages of CD8+ and interferon gamma (IFN-γ)+CD8+ gating from CD3+ cells gradually increase as the treatment outcome positively evolves from control to RSL3, to Exo and to the RSL3-Exo group, as revealed by the FCM patterns and quantitative statistical data (figure 5D,E). These results mean that RSL3-Exo indeed recruits the most infiltrations of CD8+ and IFN-γ+CD8+ T cells, which, therefore, cooperates with ITM mitigation to exert the most robust immunotherapy actions to resist tumor progression and harvest the highest inhibitory rate against 4T1 tumor growth. A similar result is obtained in the immunofluorescence assay, as shown in online supplemental figure S8, wherein the highest CD8 expression emerges in the RSL3-Exo group. Astonishingly, besides promoting M2-type macrophage polarization to mitigate ITM, Tregs (CD4+Foxp3+ cells) are also decreased (figure 5F). Such RSL3-loaded exosomes and M1-Exo give birth to the lowest Treg level, which can further support ITM mitigation and explain why immunotherapy elevation produces the inspiring antitumor outcomes. It is worth noting that RSL3-loaded exosomes induce ROS elevation, propel the accumulation of lipid peroxides and reinforce ferroptosis in the intrinsic immune cells, including M2-TAM, Tregs, CD4+ T cells and CD8+ T cells (online supplemental

figures S9–S11) since no new infiltrated immune cells were observed on the 11th day (online supplemental figure S12). In contrast, on the 21st day, the treatment with ESL3-loaded exosomes failed to influence the newly infiltrated immune cells. Afterwards, the secretion levels of protumorigenic and antitumorigenic cytokines were tested, and IFN- γ and tumor necrosis factor alpha as the tumor-resistant cytokines were significantly upregulated, and coincidentally another two tumor-supportive cytokines (eg, IL-10 and transforming growth factor beta) were rapidly decreased as the treatment outcome moved forward, as indicated in figure 5G,H. All these results uncover that the two desirable components (exosomes and RSL3) in such RSL3-loaded exosome and M1-Exo can facilitate RSL3-Exo to home to tumor, induce ferroptosis, mitigate ITM associating with M2 macrophage polarization into M1 ones and Treg downregulation, and activate and enhance systematic immune responses for inhibiting tumor progression.

The biological tissue-derived exosomes and RSL3 are two biocompatible components. Thus, it is no doubt that RSL3-Exo fails to cause evidently histopathological variations of normal organ and affect normal functions of the kidney and liver, as evidenced by no structure loss and no statistically significant fluctuation of kidney and liver indexes (online supplemental figures S13 and S14). The excellent biosafety determines that RSL3-Exo holds high clinical translation against various tumors.

CONCLUSIONS

In summary, we successfully constructed the RSL3-loaded exosome and M1-Exo (RSL3-Exo). With inheriting from parent M1 macrophages, the obtained exosomes in RSL3-Exo were validated to spontaneous home to the tumor and accumulate in the tumor in vitro and in vivo, and moreover, they could significantly promote the polarization of protumorigenic M2-type macrophages into anti-tumorigenic M1-like counterparts and decrease Tregs to mitigate ITM. More significantly, the high accumulation and mitigated ITM enabled RSL3-Exo to magnify ferroptosis via activating and enhancing the systematic immune responses and regulating ferroptosis-correlated protein expressions, which eventually acquired a desirable outcome against 4T1 tumor progression. Collectively, the biocompatible M1-Exo engineering strategy furnished a general method to successfully excise tumor immunosuppression for expediting immune-activated ferroptosis of breast tumor.

Experimental section

All materials, characterization, and experimental details have been added in the supporting information.

Supporting information available

Experimental sections including Materials and methods and online supplemental figures S1–S14 are provided in the supporting information.

Author affiliations

¹Department of Medical Ultrasound, Department of Breast, Bone and Soft Tissue Oncology, Guangxi Medical University Cancer Hospital, Nanning, Guangxi, China

²Key Laboratory of Early Prevention and Treatment for Regional High Frequency Tumor, Guangxi Medical University, Nanning, Guangxi, China

³Central Laboratory, Shanghai Tenth People's Hospital, Tongji University School of Medicine, Tongji University, Shanghai, China

⁴National Center for International Research of Bio-targeting Theranostics, Guangxi Medical University, Nanning, Guangxi, China

Contributors DW and GQ contributed equally to this work. KZ conceived this project. DW, GQ and KZ designed the experimental contents and plans. DW, GQ, XZ, QW, CZ, CF, and JL performed the experiments. KZ, DW, and YL analyzed the data. KZ and DW wrote the original manuscript, and subsequently meticulously scrutinized and revised the manuscript. YL, JL, and KZ supported and supervised the project. YL and KZ acted as guarantors. All authors commented on this article.

Funding This work was supported by Guangxi Medical University Training Program for Distinguished Young Scholars, the National Natural Science Foundation of China (grant numbers 82160341, 82022033, and 81960477), Guangxi Natural Science Foundation Key Project (2022GXNSFDA035060), the Fundamental Research Funds for the Central Universities (22120210561), and the program for Shanghai Young Top-Notch Talent.

Competing interests None declared.

Patient consent for publication Not applicable.

Ethics approval Not applicable.

Provenance and peer review Not commissioned; externally peer reviewed.

Data availability statement Data are available upon reasonable request.

Supplemental material This content has been supplied by the author(s). It has not been vetted by BMJ Publishing Group Limited (BMJ) and may not have been peer-reviewed. Any opinions or recommendations discussed are solely those of the author(s) and are not endorsed by BMJ. BMJ disclaims all liability and responsibility arising from any reliance placed on the content. Where the content includes any translated material, BMJ does not warrant the accuracy and reliability of the translations (including but not limited to local regulations, clinical guidelines, terminology, drug names and drug dosages), and is not responsible for any error and/or omissions arising from translation and adaptation or otherwise.

Open access This is an open access article distributed in accordance with the Creative Commons Attribution Non Commercial (CC BY-NC 4.0) license, which permits others to distribute, remix, adapt, build upon this work non-commercially, and license their derivative works on different terms, provided the original work is properly cited, appropriate credit is given, any changes made indicated, and the use is non-commercial. See <http://creativecommons.org/licenses/by-nc/4.0/>.

ORCID iD

Kun Zhang <http://orcid.org/0000-0002-6971-1164>

REFERENCES

- 1 Wu H, Li H, Liu Y, *et al.* Blockading a new NSCLC immunosuppressive target by pluripotent autologous tumor vaccines magnifies sequential immunotherapy. *Bioact Mater* 2022;13:223–38.
- 2 Yu X, Fang C, Zhang K, *et al.* Recent advances in nanoparticles-based platforms targeting the PD-1/PD-L1 pathway for cancer treatment. *Pharmaceutics* 2022;14:1581.
- 3 Wang D, Zhang M, Zhang Y, *et al.* Intraparticle double-scattering-decoded sonogenetics for augmenting immune checkpoint blockade and CAR-T therapy. *Adv Sci (Weinh)* 2022;9:2203106.
- 4 Yin Y, Jiang X, Sun L, *et al.* Continuous inertial cavitation evokes massive ROS for reinforcing sonodynamic therapy and immunogenic cell death against breast carcinoma. *Nano Today* 2021;36:101009.
- 5 Daurkin I, Eruslanov E, Stoffs T, *et al.* Tumor-Associated macrophages mediate immunosuppression in the renal cancer microenvironment by activating the 15-lipoxygenase-2 pathway. *Cancer Res* 2011;71:6400–9.
- 6 Bloch O, Crane CA, Kaur R, *et al.* Gliomas promote immunosuppression through induction of B7-H1 expression in tumor-associated macrophages. *Clin Cancer Res* 2013;19:3165–75.
- 7 Zhang J, Yang M, Fan X, *et al.* Biomimetic radiosensitizers unlock radiogenetics for local interstitial radiotherapy to activate systematic

- immune responses and resist tumor metastasis. *J Nanobiotechnol* 2022;20:103.
- 8 Lei L, Cai S, Zhang Y, et al. Structure inversion-bridged sequential amino acid metabolism disturbance potentiates photodynamic-evoked immunotherapy. *Adv Funct Materials* 2022;32:2103394. 10.1002/adfm.202103394 Available: <https://onlinelibrary.wiley.com/toc/16163028/32/21>
 - 9 Guan X, Yin H, Xu X, et al. Tumor metabolism-engineered composite nanoplateforms potentiate sonodynamic therapy via reshaping tumor microenvironment and facilitating electron-hole pairs' separation. *Adv Funct Mater* 2020;30:2000326. 10.1002/adfm.202000326 Available: <https://onlinelibrary.wiley.com/toc/16163028/30/27>
 - 10 Lu L, Wang T, Fang C, et al. Oncolytic impediment/promotion balance disruption by sonosensitizer-free nanoplateforms unfreezes autophagy-induced resistance to sonocatalytic therapy. *ACS Appl Mater Interfaces* 2022;14:36462–72.
 - 11 Zhang Y, Du D, Fang C, et al. Epigenetics disruptions enabled by porphyrin-derived metal-organic frameworks disarm resistances to sonocatalytic ROS anti-tumor actions. *Fundamental Research* July 2022.
 - 12 Luo T, Wang D, Liu L, et al. Switching reactive oxygen species into reactive nitrogen species by photocleaved O₂-released nanoplateforms favors hypoxic tumor repression. *Adv Sci (Weinh)* 2021;8:2101065.
 - 13 Kong F, Fang C, Zhang Y, et al. Abundance and metabolism disruptions of intratumoral microbiota by chemical and physical actions unfreeze tumor treatment resistance. *Adv Sci (Weinh)* 2022;9:2105523.
 - 14 Wang TX, Xu XH, Zhang K. Nanotechnology-enabled chemodynamic therapy and immunotherapy. *Curr Cancer Drug Targets* 2021;21:545–57.
 - 15 Zhang J, Li F, Yin Y, et al. Alpha radionuclide-chelated radioimmunotherapy promoters enable local radiotherapy/chemodynamic therapy to discourage cancer progression. *Biomater Res* 2022;26:44.
 - 16 Hou Q, Zhang K, Chen S, et al. Physical & chemical microwave ablation (MWA) enabled by nonionic MWA nanosensitizers repress incomplete MWA-arisred liver tumor recurrence. *ACS Nano* 2022;16:5704–18.
 - 17 Liu Q, Zhang W, Jiao R, et al. Rational nanomedicine design enhances clinically physical treatment-inspired or combined immunotherapy. *Adv Sci (Weinh)* 2022;9:2203921.
 - 18 Mei H, Zhang X, Cai S, et al. Fluorocarbon-driven photosensitizer assembly decodes energy conversion pathway for suppressing breast tumor. *Nano Today* 2021;41:101305.
 - 19 Song L, Lu L, Pu Y, et al. Nanomaterials-based tumor microenvironment modulation for magnifying sonodynamic therapy. *Acc Mater Res* 2022;3:971–85.
 - 20 Yang M, Zhang Y, Fang C, et al. Urine-microenvironment-initiated composite hydrogel patch reconfiguration propels scarless memory repair and reinvigoration of the urethra. *Adv Mater* 2022;34:e2109522.
 - 21 Zhang K, Fang Y, He Y, et al. Extravascular gelation shrinkage-derived internal stress enables tumor starvation therapy with suppressed metastasis and recurrence. *Nat Commun* 2019;10:5380.
 - 22 Cao H, Duan L, Zhang Y, et al. Current hydrogel advances in physicochemical and biological response-driven biomedical application diversity. *Signal Transduct Target Ther* 2021;6:426.
 - 23 Chen M, Liao H, Bu Z, et al. Pyroptosis activation by photodynamic-boosted nanocatalytic medicine favors malignancy recession. *Chemical Engineering Journal* 2022;441:136030.
 - 24 Zhang Y, Fang C, Zhang W, et al. Emerging pyroptosis-engineered nanobiotechnologies regulate cancers and inflammatory diseases: a double-edged sword. *Matter* 2022;5:3740–74.
 - 25 Tang R, Xu J, Zhang B, et al. Ferroptosis, necroptosis, and pyroptosis in anticancer immunity. *J Hematol Oncol* 2020;13:110.
 - 26 Gao W, Wang X, Zhou Y, et al. Autophagy, ferroptosis, pyroptosis, and necroptosis in tumor immunotherapy. *Signal Transduct Target Ther* 2022;7:196.
 - 27 Demuynck R, Efimova I, Naessens F, et al. Immunogenic ferroptosis and where to find it? *J Immunother Cancer* 2021;9:e003430.
 - 28 Zeng C, Tang H, Chen H, et al. Ferroptosis: a new approach for immunotherapy. *Cell Death Discov* 2020;6:122.
 - 29 Zhao L, Zhou X, Xie F, et al. Ferroptosis in cancer and cancer immunotherapy. *Cancer Commun (Lond)* 2022;42:88–116.
 - 30 Liang H, Wu X, Zhao G, et al. Renal clearable ultrasml single-crystal Fe nanoparticles for highly selective and effective ferroptosis therapy and immunotherapy. *J Am Chem Soc* 2021;143:15812–23.
 - 31 Huang Y, Zhong L, Li X, et al. In situ silver-based electrochemical oncolytic bioreactor. *Adv Mater* 2022;34:e2109973.
 - 32 Liang X, Zhang Y, Zhou J, et al. Tumor microenvironment-triggered intratumoral in situ construction of theranostic supramolecular self-assembly. *Coordination Chemistry Reviews* 2022;473:214824.
 - 33 Ren W-W, Xu S-H, Sun L-P, et al. Ultrasound-based drug delivery system. *Curr Med Chem* 2022;29:1342–51.
 - 34 Fang Y, Li H-Y, Yin H-H, et al. Radiofrequency-sensitive longitudinal relaxation tuning strategy enabling the visualization of radiofrequency ablation intensified by magnetic composite. *ACS Appl Mater Interfaces* 2019;11:11251–61.
 - 35 Zhang Y, Guo L, Kong F, et al. Nanobiotechnology-enabled energy utilization elevation for augmenting minimally-invasive and noninvasive oncology thermal ablation. *Wiley Interdiscip Rev Nanomed Nanobiotechnol* 2021;13:e1733.
 - 36 Zheng Y, Han Y, Sun Q, et al. Harnessing anti-tumor and tumor-tropism functions of macrophages via nanotechnology for tumor immunotherapy. *Exploration* 2022;2:20210166.
 - 37 Peng H, Ji W, Zhao R, et al. Exosome: a significant nano-scale drug delivery carrier. *J Mater Chem B* 2020;8:7591–608.
 - 38 Yim N, Ryu S-W, Choi K, et al. Exosome engineering for efficient intracellular delivery of soluble proteins using optically reversible protein-protein interaction module. *Nat Commun* 2016;7:12277.
 - 39 Cui Y, Guo Y, Kong L, et al. A bone-targeted engineered exosome platform delivering siRNA to treat osteoporosis. *Bioactive Materials* 2022;10:207–21.
 - 40 Ma X, Yao M, Gao Y, et al. Functional immune cell-derived exosomes engineered for the trilogy of radiotherapy sensitization. *Advanced Science* 2022;9:2106031. 10.1002/advs.202106031 Available: <https://onlinelibrary.wiley.com/toc/21983844/9/23>
 - 41 Hu S, Ma J, Su C, et al. Engineered exosome-like nanovesicles suppress tumor growth by reprogramming tumor microenvironment and promoting tumor ferroptosis. *Acta Biomater* 2021;135:567–81.
 - 42 Lu M, Xing H, Shao W, et al. Photoactivatable silencing extracellular vesicle (PASEV) sensitizes cancer immunotherapy. *Adv Mater* 2022;34:e2204765.
 - 43 Li P, Gao M, Hu Z, et al. Synergistic ferroptosis and macrophage re-polarization using engineering exosome-mimic M1 nanovesicles for cancer metastasis suppression. *Chemical Engineering Journal* 2021;409:128217.
 - 44 Li Y, Li M, Liu L, et al. Cell-Specific metabolic reprogramming of tumors for bioactivatable ferroptosis therapy. *ACS Nano* 2022;16:3965–84.
 - 45 Zhou L-L, Guan Q, Li W-Y, et al. A ferrocene-functionalized covalent organic framework for enhancing chemodynamic therapy via redox dyshomeostasis. *Small* 2021;17:e2101368.
 - 46 Gunasekaran GR, Poongkavithai Vadevoo SM, Baek M-C, et al. M1 macrophage exosomes engineered to foster M1 polarization and target the IL-4 receptor inhibit tumor growth by reprogramming tumor-associated macrophages into M1-like macrophages. *Biomaterials* 2021;278.
 - 47 Wu T, Liu Y, Cao Y, et al. Engineering macrophage exosome disguised biodegradable nanoplateform for enhanced sonodynamic therapy of glioblastoma. *Adv Mater* 2022;34:e2110364.
 - 48 Kim SB. Function and therapeutic development of exosomes for cancer therapy. *Arch Pharm Res* 2022;45:295–308.
 - 49 Liu Q, Zhang X, Zhang J. Exosome-based nanoplateforms: the emerging tools for breast cancer therapy. *Front Oncol* 2022;12:8.
 - 50 Zhang J, Ji C, Zhang H, et al. Engineered neutrophil-derived exosome-like vesicles for targeted cancer therapy. *Sci Adv* 2022;8.
 - 51 Wang P, Wang H, Huang Q, et al. Exosomes from M1-polarized macrophages enhance paclitaxel antitumor activity by activating macrophages-mediated inflammation. *Theranostics* 2019;9:1714–27.
 - 52 Zhang Y, Yin Y, Zhang W, et al. Reactive oxygen species scavenging and inflammation mitigation enabled by biomimetic Prussian blue analogues boycott atherosclerosis. *J Nanobiotechnol* 2021;19:161.
 - 53 Dai E, Han L, Liu J, et al. Autophagy-Dependent ferroptosis drives tumor-associated macrophage polarization via release and uptake of oncogenic KRAS protein. *Autophagy* 2020;16:2069–83.
 - 54 Liu J, Zhang Z, Yang Y, et al. NCOA4-mediated ferroptosis in bronchial epithelial cells promotes macrophage M2 polarization in COPD emphysema. *COPD* 2022;Volume 17:667–81.

Supporting information for

**Macrophage-Inherited Exosome Excise Tumor Immunosuppression to Expedite
Immune-Activated Ferroptosis**

Duo Wang,[#] Guanhua Qiu,[#] Xiaoqi Zhu, Qin Wang, Chunyan Zhu, Chao Fang, Junjie Liu, Kun
Zhang* and Yan Liu*

Experimental sections

Extraction of primary born-derived macrophages

8-week-old BALB/C mice of SPF grade were killed by cervical dislocation. Bone marrow derived macrophages (BMDM) were isolated from tibias and femurs of mice, and then cultured in DMEM supplemented with macrophagecolony stimulating factor (HY-P7361, MedChenExpress, USA) and 10% fetal bovine serum (FBS) for 7 days. And then, cells were incubated with DMEM supplemented with lipopolysaccharide (LPS) (1 µg/mL, HY-D1056, MedChenExpress, USA) 24 h - 48 h for M1 polarization.

Macrophage-derived exosomes (Exo) isolation and RSL3-Exo preparation

Primary born-derived macrophages cells were cultured with exosome-depleted 10% FBS and the supernatant was collected (about 200 mL). Then, low-speed centrifugation was used in turns: 300 g centrifugal for 10 min, 2000 g centrifugal for 15 min and 10000 g centrifugation for 30 min to remove cell fragments and larger microbubbles. Finally, 100000 g ultracentrifugation for 90 min twice was carried out to remove protein impurities and separate the purified exosome. The exosomes were resuspended in 100 µL of cold Duchenne phosphate buffer solution (DPBS) and preserved to -80 °C. In the above operation, all centrifugations were carried out at 4 °C.

The protein content of the exosome was detected by protein quantitative kit (P0012S, Beyotime, China), and then verified the exosome markers (CD9, CD63, CD81, Alix, Calnexin and β-Actin) by western blot. The protein of exosomes (20 µg) was added to the SDS sample buffer, electrophoretic and transferred to the PVDF membrane, and then analyzed by anti-CD9 (A19027, ABclonal, China), anti-CD63 (A19023, ABclonal, China), anti-CD81 (A5270, ABclonal, China), anti-Alix (A2215,

ABclonal, China), anti-Calnexin (A15631, ABclonal, China) and β -Actin antibody (AC006, ABclonal, China).

In order to prepare RSL3-Exo, RSL3 (1219810-16-8, Aladdin, China) (Molecular Weights: 440.88) was mixed with exosomes (1 mg/mL, 1 mL) in DPBS solution into a cell culture dish through shaking overnight at 4 °C. Then, after removing extra RSL3 by centrifugation, the supernatants were collected and stored in cold DPBS solution for further use.

Characterizations

To analyze particle shape of the extracted exosome using a transmission electron microscope (TEM) (Tokyo, Japan); Nanoparticle tracking analysis (NTA) was performed to measure the size of the exosome (Nanosight, Malvern, UK).

Cell lines and animals

Murine breast cancer cell line (4T1), Murine colon tumor cell line (CT26) were purchased from the American type culture collection (ATCC) (Manassas, VA, USA). The cells were cultured in a humidified incubator at 37 °C and 5% CO₂ atmosphere under the optimum conditions. BALB/C mice were purchased from SPF Biotechnology Inc. (Beijing, China). Mice were maintained in accordance with the Guidelines of the Institutional Animal Care and Use Committee of Guangxi Medical University. All animal experiments have been approved by the Animal Care and Use Committee of Guangxi Medical University with an approval number: LW2022172.

Colony formation assay

For colony formation survival assays, a total of 5×10^2 4T1 and CT26 cells in the logarithmic growth phase were seeded into 6-well plates, the cells were cultured with four following groups (RSL3: 0.5 μ g/mL, Exosome: 10 μ g/mL): G1 Control (PBS); G2 RSL3; G3 Exo; G4 RSL3-Exo. 14 days later,

after PBS cleaning, the cells were fixed in methanol and stained with 0.5% crystal violet. The cells were counted under a microscope.

Internalization of exosomes

A total of 1×10^5 4T1 cells in the logarithmic growth phase were seeded into special culture dish. After cultured overnight, DiD near-infrared dye-labeled RSL3-Exo was added to the dishes at 0 h, 2 h, 4 h, 6 h (RSL3: 0.5 $\mu\text{g}/\text{mL}$, Exosome: 10 $\mu\text{g}/\text{mL}$). Then stained the cells by Hoechst 33342 (C1025, Beyotime, China) for 15 minutes, used cold PBS to wash 3 times, then the cells were immediately observed using confocal laser scanning microscopy (CLSM) (Leica SP8, Germany) (the wavelength of excitation and emission is 346 nm / 460 nm (Hoechst 33342), 646 nm / 663 nm (DiD near-infrared)).

Measurement of ROS

A total of 1×10^6 4T1 and CT26 cells in the logarithmic growth phase were seeded into 6-well plates, the cells were cultured with four following groups (RSL3: 0.5 $\mu\text{g}/\text{mL}$, Exosome: 10 $\mu\text{g}/\text{mL}$) for 12 h: G1 Control (PBS); G2 RSL3; G3 Exo; G4 RSL3-Exo. Cells were incubated with 1:1000 diluted DCFH-DA probes (S0033M, Beyotime, China) in a cell incubator (37 °C, 5% CO₂) for 20 min, washed with cold PBS 3 times. Images were visualized on an inverted fluorescence microscope (the wavelength of excitation and emission is 488 nm / 525 nm).

GSH detection

A total of 1×10^6 4T1 and CT26 cells in the logarithmic growth phase were seeded into 6-well plates, the cells were cultured with four following groups (RSL3: 0.5 $\mu\text{g}/\text{mL}$, Exosome: 10 $\mu\text{g}/\text{mL}$) for 12 h: G1 Control (PBS); G2 RSL3; G3 Exo; G4 RSL3-Exo. Cells were incubated with 1:1000 diluted ThiolTracker (T10096, Thermo Fisher, USA) in a cell incubator (37 °C, 5% CO₂) for 20 min,

washed with cold PBS 3 times. Images were visualized on an inverted fluorescence microscope (the wavelength of excitation and emission is 405 nm / 525 nm).

Lipid peroxidation assay

A total of 1×10^6 4T1 cells in the logarithmic growth phase were seeded into 6-well plates, the cells were cultured with four following groups (RSL3: 0.5 $\mu\text{g}/\text{mL}$, Exosome: 10 $\mu\text{g}/\text{mL}$) for 12 h: G1 Control (PBS); G2 RSL3; G3 Exo; G4 RSL3-Exo. Cells were incubated with 1:1000 diluted C₁₁-BODIPY (D3861, Thermo Fisher, USA) in a cell incubator (37 °C, 5% CO₂) for 1 h, washed with cold PBS 3 times. Images were visualized on an inverted fluorescence microscope (In reduced state, the wavelength of excitation and emission is 581 nm / 591 nm; after oxidation, the wavelength of excitation and emission is 488 nm / 510 nm).

Analysis of dead and living cells stained with Calcein AM / PI

A total of 1×10^6 4T1 and CT26 cells in the logarithmic growth phase were seeded into 6-well plates, the cells were cultured with four following groups for (RSL3: 0.5 $\mu\text{g}/\text{mL}$, Exosome: 10 $\mu\text{g}/\text{mL}$) 12 h: G1 Control (PBS); G2 RSL3; G3 Exo; G4 RSL3-Exo. Cells were incubated with 1:1000 diluted Calcein AM / Propidium Iodide (PI) (C2015M, Beyotime, China) in a cell incubator (37 °C, 5% CO₂) for 10 min, and then washed with cold PBS 3 times. Images were recorded on an inverted fluorescence microscope (Green fluorescence representing live cells: the wavelength of excitation and emission is 494 nm / 517 nm; and red fluorescence representing dead cells: the wavelength of excitation and emission is 535 nm / 617 nm).

Flow cytometry analysis

A total of 1×10^6 4T1 cells in the logarithmic growth phase were seeded into 6-well plates, and these cells were cultured in the following four groups for 12 h (RSL3: 0.5 $\mu\text{g}/\text{mL}$, Exosome: 10 $\mu\text{g}/\text{mL}$),

i.e., G1: Control (PBS), G2: RSL3 alone, G3: Exo alone, G4: RSL3-Exo, respectively. Cells and supernatant were collected after centrifugation, and 200 μL of PBS was used to resuscitate cells. Cells were incubated with 5 μL of Annexin V-FITC, 10 μL of PI (C1062S, Beyotime, China) in a cell incubator (37 $^{\circ}\text{C}$, 5% CO_2) for 20 min. A CytoFLEX S flow cytometer (Beckman Coulter, China) and FlowJo software (Version10.5.3, TreeStar) were used for further analyses.

Animal models and anti-tumor therapy

4-5 weeks old BALB/C female mice were randomly divided into 4 groups (n=5): G1: Control (PBS), G2: RSL3, G3: Exo, G4: RSL3-Exo. A total of 1×10^6 4T1 cells were injected subcutaneously into the left lower limb of the mice, until the diameter of the tumor was about 5 mm, all mice were treated by injecting into the mice via the tail vein. (200 μL , RSL3: 3 mg/kg, Exosome: 60 mg/kg, every other day, a total of five injections). Tumor sizes were measured using a digital caliper every 3 days. At the same time, the weight of mice was measured by electronic scale. The tumor volume in mm^3 was calculated using the following formula:

$$\text{Tumor volume} = \frac{L \times W \times W}{2}$$

In the formula, L is the longest dimension and W is the perpendicular dimension. After 11 and 21 days post-corresponding treatment, respectively, the mice were sacrificed and collected the mice subcutaneous tumor tissue for flow cytometry, ELISA, immunofluorescence staining, WB; and the mice spleen tissue for H&E staining.

Blood samples were collected for ELISA testing. As well, another 20 mice were divided into the same groups (n=5) as mentioned above and received the same treatments for survival analysis. This was defined as the end point when the tumor volume reached 1000 mm^3 or the mice died prematurely.

In vivo fluorescence imaging

When the tumors reached 200 mm³, 4T1 tumor-bearing BALB/C mice after anesthesia with isoflurane were injected with ICG-labeled RSL3 (200 µL, Exosome: 60 mg/kg) via tail vein. After injection for 2 h, 6 h, 12 h, 24 h and 48 h, the mice tumors were positioned at the center of the scanning horizon and imaged using the fluorescence imaging instrument (PIXIS 1024, Princeton, USA) (the wavelength of excitation and emission is 785 nm / 840 nm). After being treated for 48 h, mice were sacrificed. The tumors and some main organs (heart, liver, spleen, lung and kidney) were collected to observe the distribution of ICG-Exo in tumor and main organs by fluorescence instrument.

Western blot analysis

WB was used to detect the change of Glutathione Peroxidase-4 (GPX4) protein expression in 4T1 cells and Cytochrome C, Caspase3, Caspase9, Poly ADP-Ribose Polymerase (PARP) protein expression in tumor tissue (4T1 bearing-tumor), and the GPX4 protein expression in CD4, CD8, Treg, M2 Macrophage after 11 and 21 days post-corresponding treatment. Four groups were set, i.e., G1 Control (PBS); G2 RSL3; G3 Exo; G4 RSL3-Exo. After corresponding treatment, proteins were extracted from cells and tumor tissues by RIPA Lysis Buffer (P0013B, Beyotime, China). Then the proteins were subjected to electrophoresis using 10% polyacrylamide gels and transferred onto PVDF membranes, and analyzed by GPX4 (A1933, ABclonal, China), anti-Cytochrome C (A4912, ABclonal, China), anti-Caspase-3 (9661, Cell Signaling Technology, USA), anti-Caspase-9 (A22672, ABclonal, China), anti-PARP (9532, Cell Signaling Technology, USA) and GAPDH antibody (AC001, ABclonal, China).

Measurements of cytokines level by ELISA

Four groups were set, i.e., G1: Control (PBS), G2: RSL3, G3: Exo, G4: RSL3-Exo. 4T1 tumor-bearing BALB/C mice after corresponding treatment, and blood sample was collected from the eyeballs. The concentrations of IL-10 (EMC005, Neobioscience, China), TNF- α (EMC102a, Neobioscience, China), TGF- β (EMC107b, Neobioscience, China) and IFN- γ (EMC101g, Neobioscience, China) in proteins which extracted from tumor tissues were detected by ELISA kit (Neobioscience, China).

Flow cytometry analysis for tumor

Four groups were set, i.e., G1: Control (PBS), G2: RSL3, G3: Exo, G4: RSL3-Exo. After 21 days post-corresponding treatment, the 4T1 tumors implanted in BALB/C mice were quickly excised and mechanically dissociated in PBS with scissors, and continuously rinsed with PBS solution to release tumor infiltrating lymphocytes, followed by single cell suspension collection. Centrifugation for 7 min at 1500 rpm was carried out, and then the cells were re-suspended with percoll. Afterwards, the centrifugation for 15 min at 600 g was implemented to collect single-cell suspension. After that, TILs in tumor tissues was stained with CD45-APC-CY7, CD3-PerCP-CY5.5, CD8-PE-CY7, CD4-BV510, Foxp3-APC, IFN- γ -BV421 or CD45-APC-CY7, F4/80-PerCP-CY5.5, CD86-BV510, CD206-PE-CY7, which were obtained from Biolegend, USA.

Isolation and extraction of tumor infiltrating immune cells

After 11 days and 21 days post-treatments with RSL3 or RSL3-Exo, respectively, 4T1 tumors implanted in BALB/C mice were quickly excised and mechanically dissociated in PBS with scissors, then centrifuged, re-suspended and collected single-cell suspension. Subsequently, CD3-PerCP-CY5.5, CD8-PE-CY7, CD4-BV510, Foxp3-APC or F4/80-PerCP-CY5.5,

CD206-PE-CY7 antibodies were added and incubated with the TILs, followed by magnetic bead sorting and ROS determination by the probe (DCFH-DA probes-FITC) (S0033M, Beyotime, China) on FCM.

Detection of malondialdehyde (MDA) content

After 11 days and 21 days post-treatments with RSL3 or RSL3-Exo, respectively, 4T1 tumors implanted in BALB/C mice were quickly excised and mechanically dissociated in PBS with scissors, and continuously rinsed with PBS solution to release tumor infiltrating lymphocytes, followed by single cell suspension collection. Centrifugation for 7 min at 1500 rpm was carried out, and then the cells were re-suspended with percoll. Afterwards, the centrifugation for 15 min at 600 g was implemented to collect single-cell suspension. CD3-PerCP-CY5.5, CD8-PE-CY7, CD4-BV510, Foxp3-APC or F4/80-PerCP-CY5.5, CD206-PE-CY7 antibodies (Biolegend, USA) were added and incubated with the tumor infiltrating lymphocytes, followed by magnetic bead sorting to collect the CD4⁺ T cells, CD8⁺ T cells, Tregs and M2 macrophages, After that, the cells were seeded in 6-well plates and the supernatant was collected to detect the concentration of MDA (RQ-E20347, Ruiqing, China) by ELISA kit where MDA as the end product of lipid peroxide was used to evaluate the accumulation of lipid peroxide.

Immunofluorescence analysis of tissues

Frozen tumor tissue (8- μ m thickness) were incubated with TUNEL (C10618, ThermoFisher, USA), ROS probe (BES20246BO, Biosn, China), anti-GPX4 (AF7020, Beyotime, China), anti-CD3 (GB111337, Servicebio, China) and anti-CD8 (GB11068, Servicebio, China) antibodies at 4 °C overnight and then with secondary antibody (ThermoFisher Scientific, USA). Tissue samples were

counterstained with DAPI, and observed using confocal laser scanning microscopy. Meanwhile, the tumor tissues were embedded in paraffin, sectioned, and stained with hematoxylin and eosin (H&E).

Safety evaluation in vivo

Four to five-week-old BALB/C female mice were randomly divided into 2 groups (n=3), i.e., G1: Control (PBS) and G2: RSL3-Exo. The mice in RSL3-Exo group were injected with RSL3-Exo via the tail vein (200 μ L every other day, a total of five injections, RSL3: 3 mg/kg, Exosome: 60 mg/kg). The body weight and temperature of mice were monitored every 10 days. After 5 days, 15 days, 25 days, blood was collected from the eyeballs, followed by blood biochemical tests and liver & kidney function tests (red blood cells, white blood cells, platelets, aspartate aminotransferase, alanine aminotransferase, lactate dehydrogenase, creatinine, urea and creatine kinase). Main organs (heart, lung, brain, liver, spleen, kidney, stomach and intestine) were stained with H&E and photographed for observation.

Statistical assessment

All data were presented as the mean \pm standard deviation (SD), where n =3 that means at least three independent experiments is routine unless otherwise indicated in the figure legend. Statistical analysis was performed with IBM SPSS V.24.0 software. Statistical significance was determined using ANOVA. Two-sided p values less than 0.05 were considered to be statistically significant, and *P<0.05, **P<0.01 and ***P<0.001. All statistical analyses were performed with GraphPad Prism software (version 9.0).

Supplementary figures

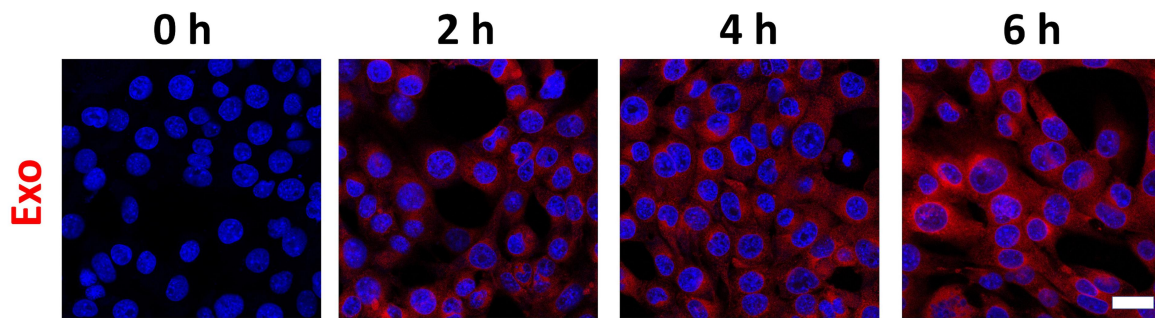


Figure S1 CLSM images of 4T1 cells after incubation with DiD-labeled RSL3-Exo for different time durations, and Scale bar: 20 μ m.

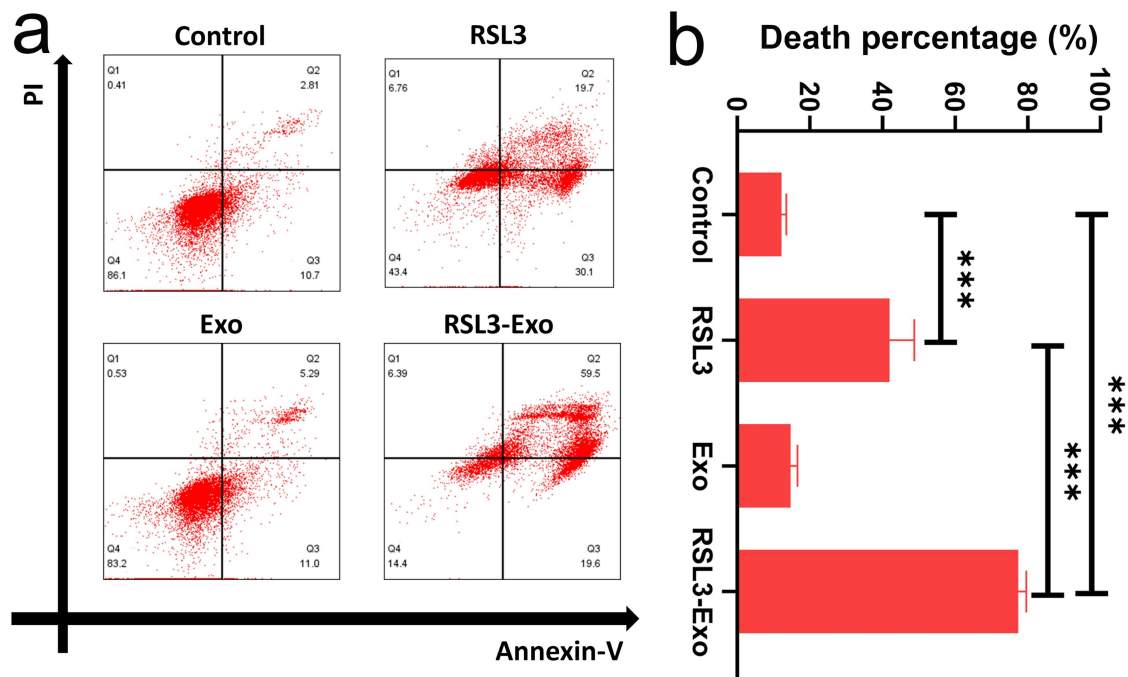


Figure S2 (a) FCM patterns of 4T1 cells stained with PI and Annexin-V after different treatments in their corresponding groups; and (b) the quantitative percentage. Data are expressed as mean \pm SD (n=3). The One-way ANOVA was used to analyse the statistical differences between two groups, and ***P<0.001.

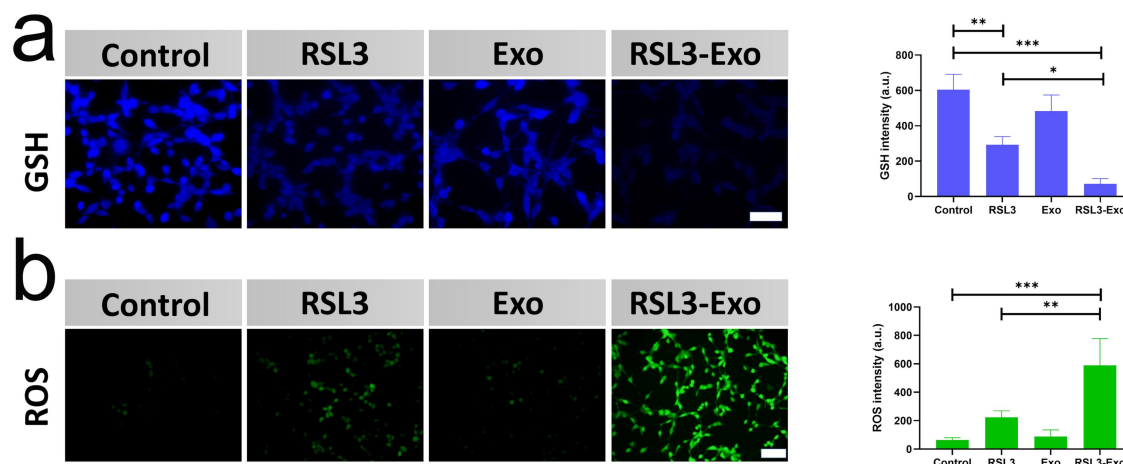


Figure S3 (a,b) CLSM images and quantitative level of GSH level (a) and ROS level (b) in CT26 cells stained with GSH and ROS indicators after different treatments in their corresponding groups. Scale bar: (a) 50 μ m, (b) 100 μ m. Data are expressed as mean \pm standard deviation (SD, n=3). The One-way ANOVA was used to analyze the statistical differences between two groups, and * $P < 0.05$, ** $P < 0.01$ and *** $P < 0.001$.

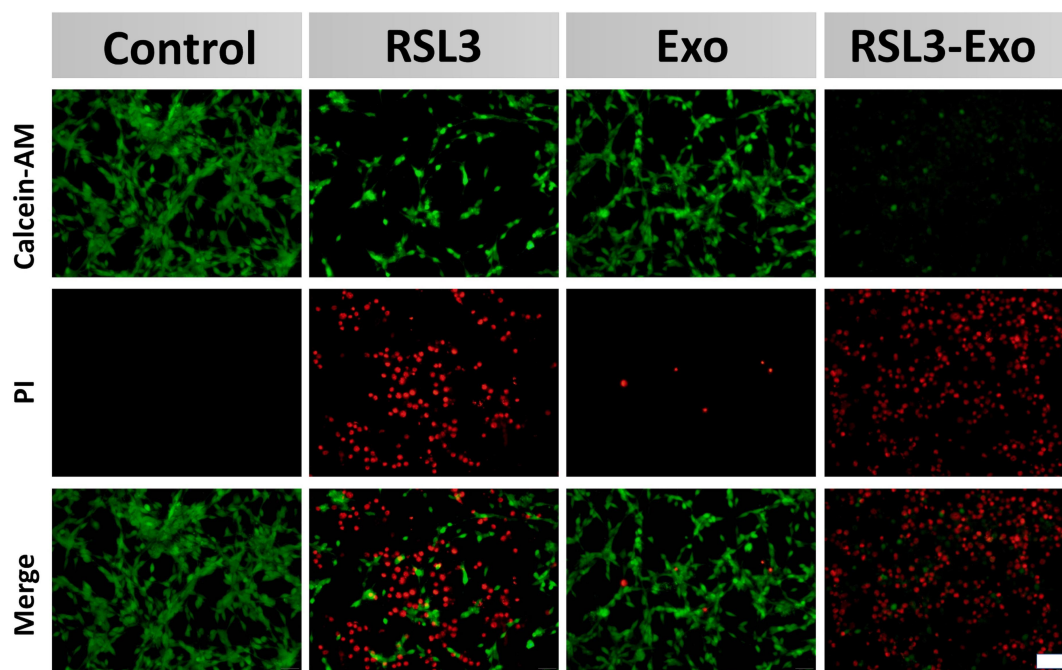


Figure S4 CLSM images of CT26 cells stained with live/dead dyes (i.e., PI/Calcein-AM) after different treatments in their corresponding groups, where PI-stained red cells and Calcein-AM-stained green cells indicate dead and live cells, respectively. Scale bar: 100 μ m.

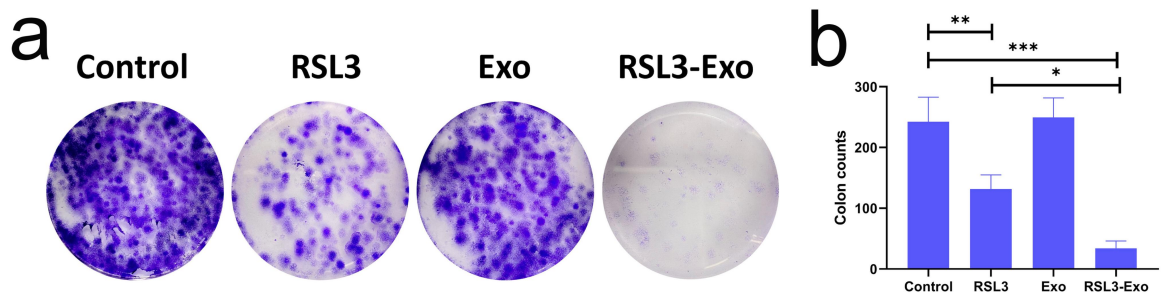


Figure S5 Clone tests for detecting proliferation level of CT26 cells after different treatments in their corresponding groups including via optical microscopic observation (a) and quantitative verification (b). Data are expressed as mean \pm standard deviation (SD, n=3). The One-way ANOVA was used to analyze the statistical differences between two groups, and * $P < 0.05$, ** $P < 0.01$ and *** $P < 0.001$.

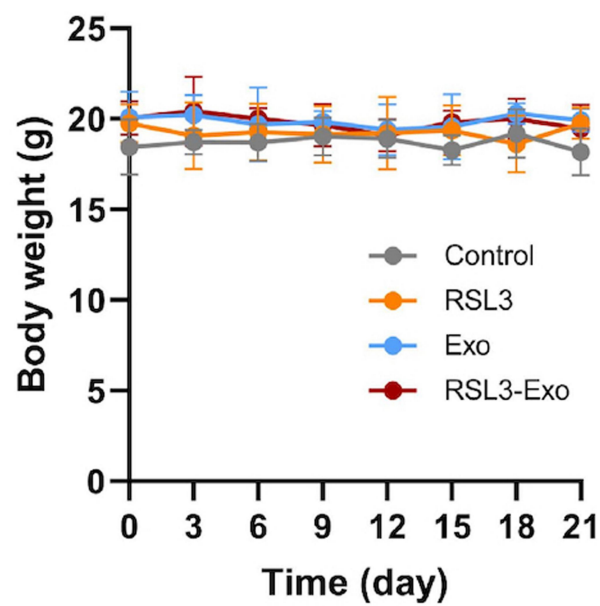


Figure S6 The time-correlated body weight variation profiles of 4T1 tumor-bearing mice after the corresponding treatments in each group. Data are expressed as mean \pm SD (n=5).

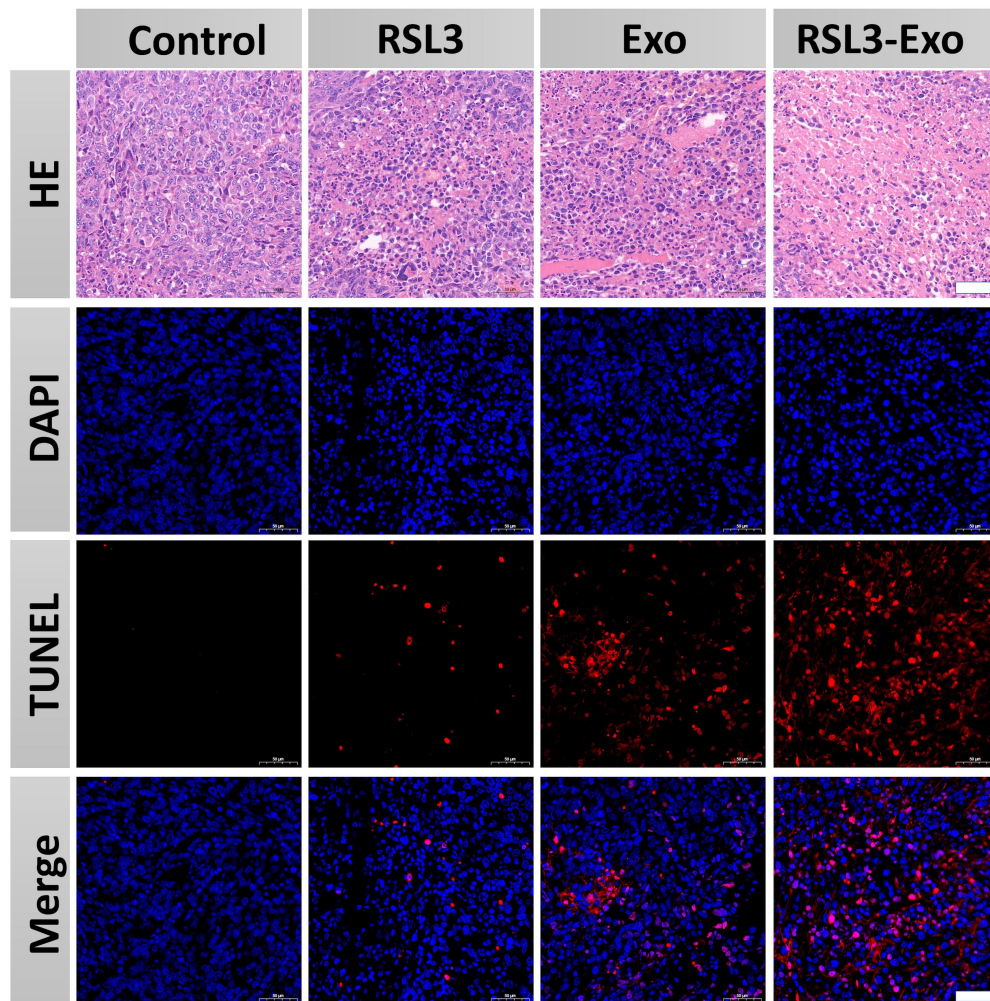


Figure S7 H&E immunohistochemical and TUNEL immunofluorescence images of 4T1 tumor slices, which were collected from 4T1 tumor-bearing mice that experienced different treatments in the corresponding groups, and scale bar: 50 μ m.

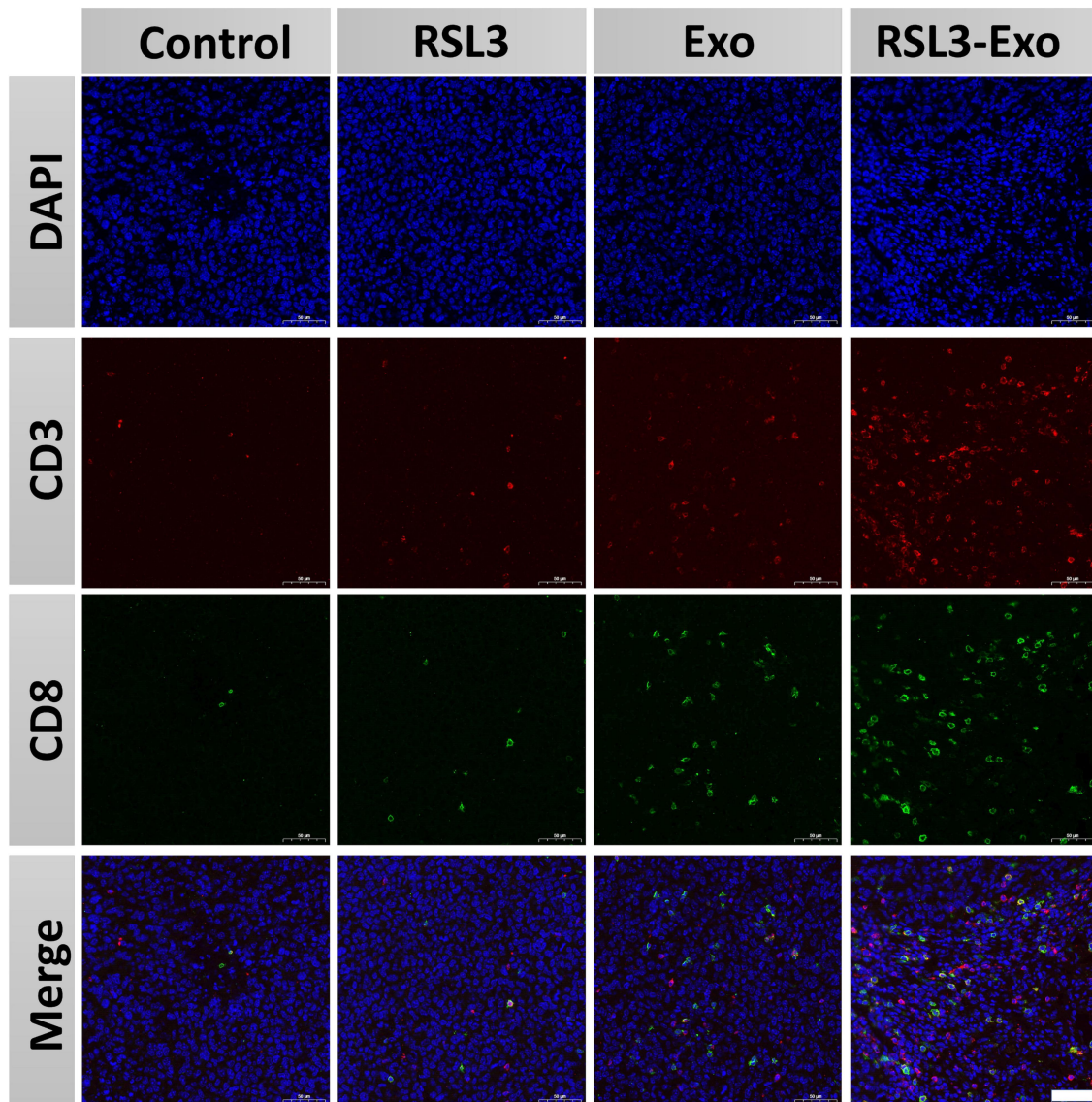


Figure S8 CLSM images of 4T1 tumor slices stained with anti-CD3 and anti-CD8 antibodies, which were collected from 4T1 tumor-bearing mice that experienced different treatments in the corresponding groups, and scale bar: 50 µm.

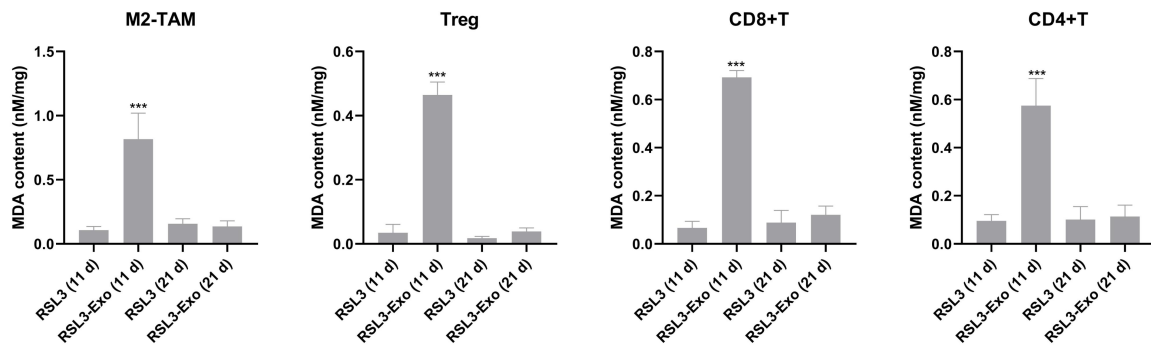


Figure S9. ELISA data of MDA in different immune cells including M2-TAM, Tregs, CD8+T cells and CD4+T cells after 11 days and 21 days post-treatments with RSL3 alone and RSL3-Exo, respectively. Data are expressed as mean±SD (n=3), and ***P < 0.001.

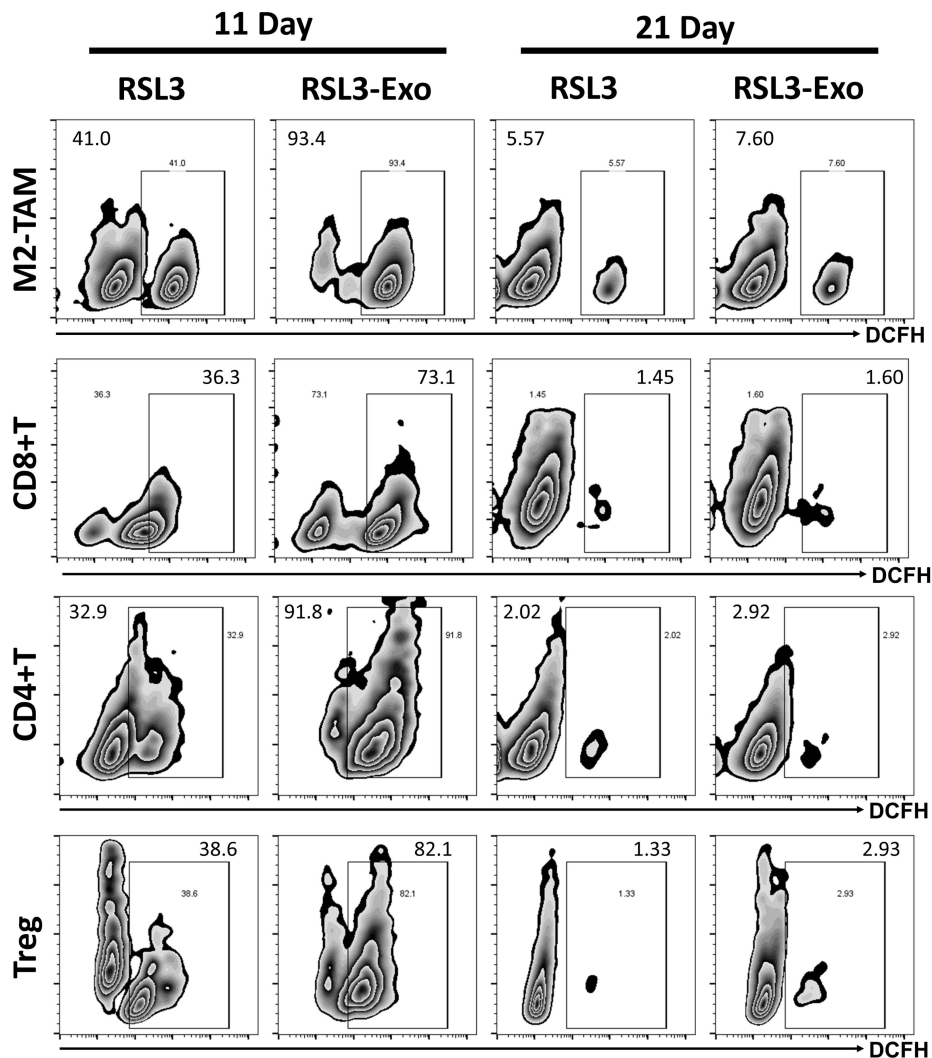


Figure S10. FCM patterns of ROS-positive M2-TAM, CD8+T cells, CD4+T cells and Tregs after 11 days and 21 days post-corresponding treatments in the four groups (i.e., Control, RSL3, Exo and RSL3-Exo).

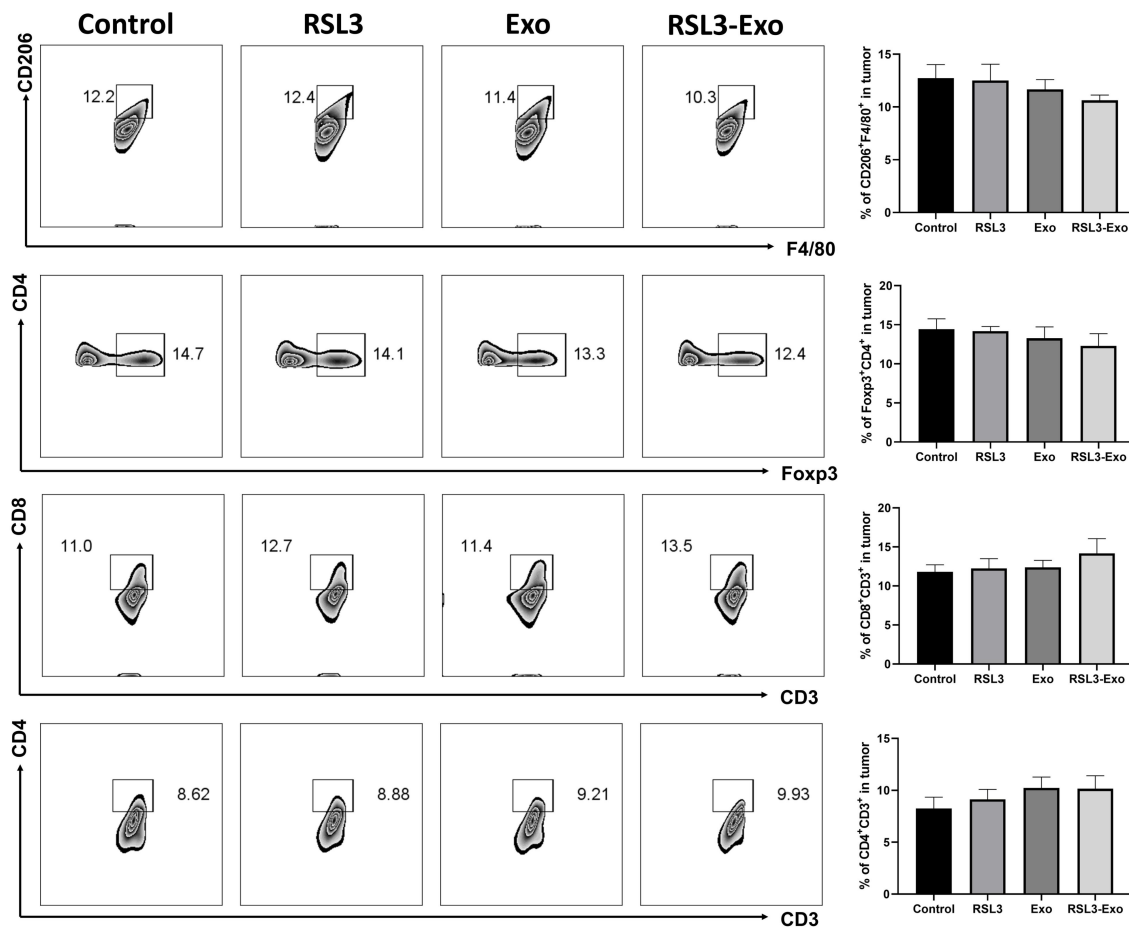


Figure S11. FCM patterns and quantitative levels of CD206⁺ (M2-TAM), CD4⁺FOXP4⁺ (Tregs), CD8⁺ T cells and CD4⁺T cells after 11 days post-corresponding treatments in the four groups (i.e., Control, RSL3, Exo and RSL3-Exo). Data are expressed as mean \pm SD (n=3).

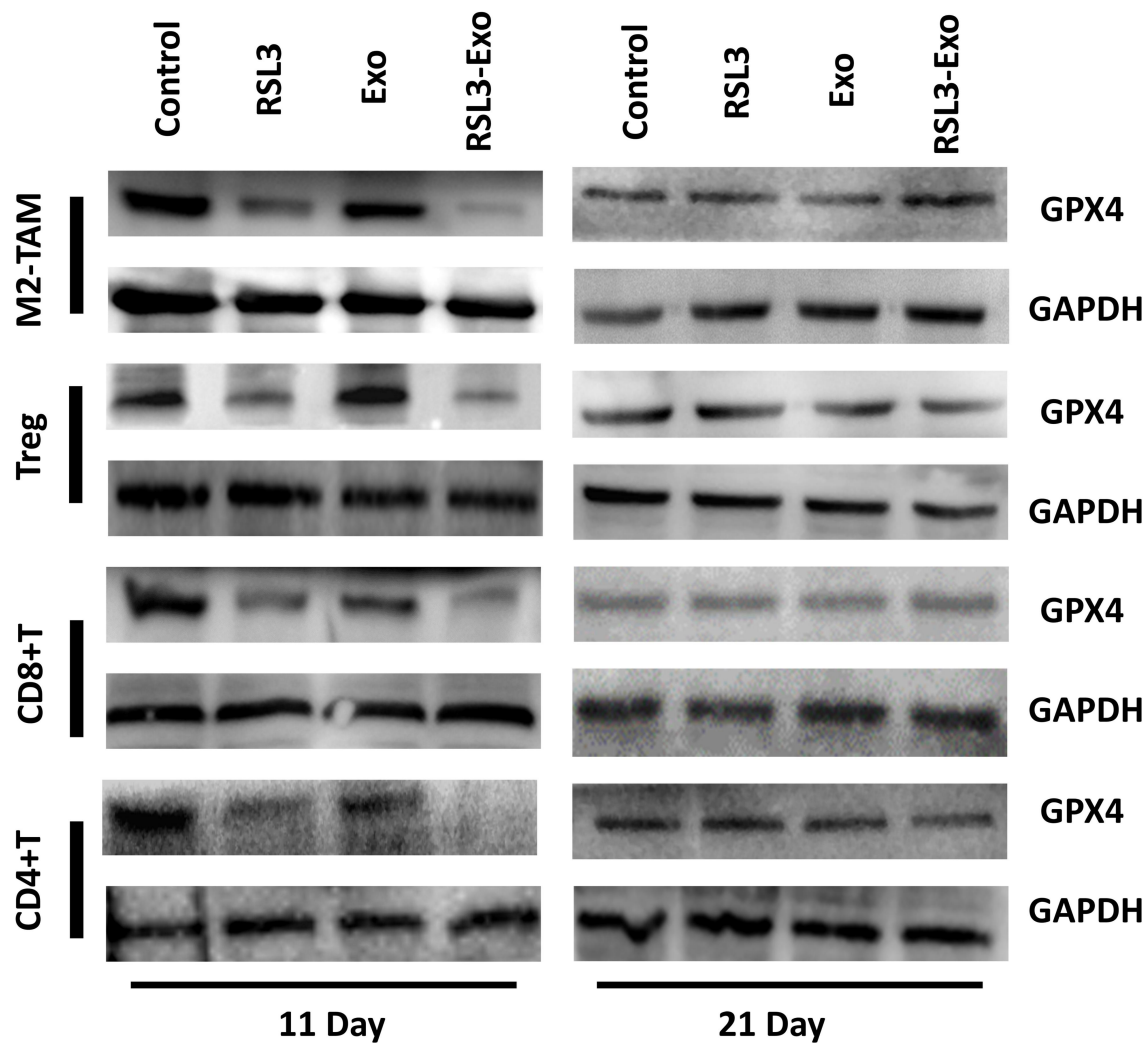


Figure S12. WB patterns of GPX4 proteins in different immune cells (e.g., M2-TAM, Tregs, CD8+T cells and CD4+T cells) after 11 days and 21 days, respectively, wherein GPX4 represents the ferroptosis.

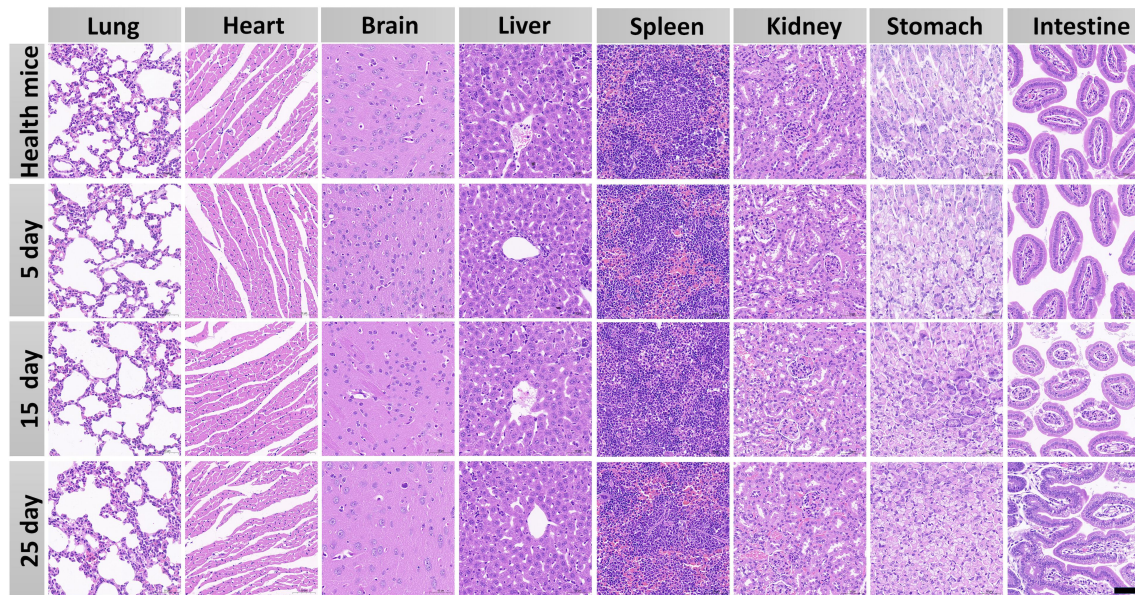


Figure S13 Time-dependent H&E immunohistochemical images of various organs collected from 4T1 tumor-bearing mice that experienced different treatments in the corresponding groups, and scale bar: 50 μm .

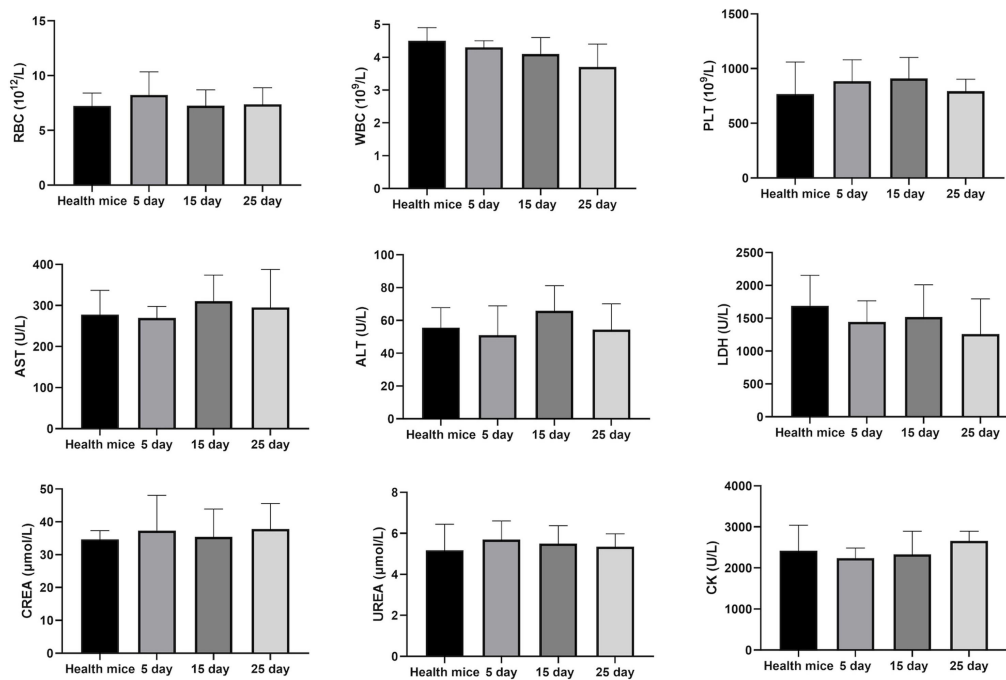


Figure S14 Blood and biochemical indexes for evaluating liver and kidney function variations in both healthy mice and treated mice with RSL3-Exo for different periods (5 days, 15 days and 25 days). Data are expressed as mean \pm SD (n=3).